Jawahar Education Society's,
**INSTITUTE OF TECHNOLOGY,
MANAGEMENT & RESEARCH, NASHIK.**

3.2.1   Number of papers published per teacher in the Journals notified on UGC website during the year.

Sr. No	Title of paper	Name of the author/s	Department of the teacher	Name of journal	Year of publication	ISSN number	Click on Page Number
1	Investigations And Optimization Of Laser Process Parameters Using Box Benhken Design Approach For Advanced Materials	Mr. Sagarkumar J. Aswar	Department of Mechanical Engineering	Journal Of Aeronautical Materials	2023	ISSN: 1005-5053	**02**
2	Experimental Analysis On Laser Cutting Of Hastelloy C 276: Effects Of Process Parameters On Kerf Width, Surface Roughness, Haz Using Taguchi Technique	Mr. Sagarkumar J. Aswar	Department of Mechanical Engineering	Journal Of Aeronautical Materials	2023	ISSN: 1005-5053	**20**
3	Finite Element Modelling of Laboratory Tests on Reinforced Concrete Beams Containing Recycled Aggregate Concrete	Mr. A. J. Pawar	Department of Civil Engineering	International Journal of Engineering	2023	ISSN:1728-144X	**33**
4	Constrained Static/Dynamic Economic Emission Load Dispatch Using Elephant Herd Optimization	Mrs. Swati K. Warungase	Department of Electrical Engineering	Information 2023	Jun-23	e-ISSN: 2078-2489	**42**

INVESTIGATIONS AND OPTIMIZATION OF LASER PROCESS PARAMETERS USING BOX BENHKEN DESIGN APPROACH FOR ADVANCED MATERIALS

Sagarkumar J Aswar[1], Nilesh Diwakar[2], S. D. Kalpande[3]

[1]Ph.D. Research Scholar, RKDFIST, SRK University, Bhopal, India.
[2]Prof., Department of Mechanical Engineering, RKDFIST, SRK University, Bhopal, India.
[3]Prof., Department of Mechanical Engineering, GCOERC, Nashik, India.

Corresponding author: Sagarkumar J. Aswar, sagaraswar123@gmail.com

Abstract:

This paper presents the results of an experimental study conducted to identify the parameters of the laser machining process that yield the best results when working with Hastelloy C276, a nickel-based alloy commonly used in the aerospace, defense, energy, and food processing industries. Laser cutting is a non-contact thermal cutting process that uses a high-power laser beam to melt and vaporize the material. The Box-Behnken design with ANOVA analysis was utilized to determine the impact of laser machining process parameters (laser power, cutting speed, and gas pressure) on Heat-Affected Zone (HAZ) and surface roughness (Ra). Applying specific optimization techniques, a set of approximate optimal parameters was obtained. According to the results, a laser with a power of 2400 watts, gas pressure of 15.66 bar and cutting speed of 2232.58 mm/min yielded machined components with the best possible quality and efficiency, with a surface roughness of 0.78 (μm), HAZ of 0.127 mm. Overall, the Box-Behnken design approach with response surface methodology (RSM) is a powerful tool that can be used to optimize laser machining process parameters for the material Hastelloy C-276 sheet. With this approach, the process parameters can be adjusted to yield the desired performance and quality of the machined parts. Furthermore, the results of this study demonstrate the importance of setting the laser power to the optimal value in order to achieve the best results.

Key words: Heat affected zone (HAZ), Surface roughness (Ra), Laser power, Cutting speed, Gas pressure

1. INTRODUCTION

Hastelloy is a family of nickel-based alloys that contain varying amounts of molybdenum, chromium, and other elements to provide high strength, corrosion resistance, and heat [1]. These properties make Hastelloy ideal for use in harsh environments such as chemical processing, oil and gas production, and aerospace [2]. It has also been a highly attractive material for naval/marine applications [3]. Laser cutting is a precise and efficient cutting method that has gained popularity in recent years due to its ability to cut a wide range of materials with high accuracy and speed [4]. Laser cutting of Hastelloy has unique challenges due to its high melting point, low thermal conductivity, and tendency to form a hard and brittle heat-affected zone (HAZ) during cutting [5]. In this research paper, we will explore the recent

developments in laser cutting of Hastelloy and the potential applications of this process in various industries. Compared to traditional cutting methods such as plasma cutting or water jet cutting, laser cutting has several advantages when it comes to cutting Hastelloy [6,7]. As a first advantage, laser cutting does not involve any motorized power or touch with the material being removed [8-10]. Second, laser cutting produces a narrow kerf width and a small HAZ, resulting in minimal material waste and distortion. Third, laser cutting can achieve high cutting speeds and accuracy, making it suitable for mass production and complex geometries [11]. However, laser cutting of Hastelloy has limitations. The high energy input of the laser beam can cause melting, vaporization, and oxidation of the material, leading to surface roughness, cracking, and porosity [12-14]. In addition, the thermal stress induced by the laser beam can cause distortion and residual stress in the material. The quality of laser cutting for Hastelloy depends on various process parameters such as laser power, cutting speed, focal position, assist gas, and nozzle diameter [15]. The laser power determines the amount of energy delivered to the material, affecting the cutting depth, kerf width, and edge roughness [16]. The cutting speed affects the heat input and cooling rate of the material, influencing the microstructure and HAZ width. The focal position determines the focus diameter and shape of the laser beam, affecting the spot size and energy density at the cutting surface. The assist gas, usually nitrogen or oxygen, helps to remove the molten material and protect the cutting zone from oxidation [17-19]. The nozzle diameter affects the gas flow rate and pressure, affecting the gas flow pattern and the shape of the molten pool. To improve Hastelloy C-276's wear resistance [20] used laser surface treatment in an argon atmosphere, where they found the adjusting the laser's specifications to produce a hard, durable layer without annealing in advance is a method to achieve it. Ra and HAZ were measured after being machined from Inconel 718, a nickel-based superior alloys, to determine the impacts of various laser cutting parameters. employing an X-ray and a scanning electron microscope. CO_2 laser cutting process factors which enhance Ra, HAZ, kerf width, and material removal rate (MRR) when machining stainless steel were investigated using a preference selection index [21]. Used experimental data and the RSM method to do a statistical analysis While machining sheets of polycarbonate with a laser, the properties "Ra and geometry" are influenced by the process parameters of the laser, which include the laser power, the rate of cutting, and the focal location. In order to get a high frequency cut while employing a Nd:YAG laser with pressurized gas, a multi-objective optimization of the kerf deviation, kerf width, and kerf taper [24]. Parametric studies conducted on laser machining processing parameters such as laser power, cutting speed, and gas pressure discovered that laser power seems to have a significant impact on Ra and top kerf when working with stainless steel (ASTM 304) [25]. Particle swarm optimization, a swarm-based optimization method, was used to optimize the objective function, i.e., the geometrical quality, of a test done on Inconel-718 to use a pulsed Nd: YAG laser beam. [26] is being carried out research in order to examine the quality of laser cutting in relation to the processing parameters of CO_2 laser cutting for the aluminum alloy AA5083. These processing parameters include laser power, scanning speed, pulse frequency, and the gas pressure. Joshi et al., [27] carried out a study to use a pulsed Nd-YAG laser and a Box-Behnken design to investigate kerf geometry and metallurgical variation in resource aluminum alloy (Al 6061-T6) with selected settings of lamp current, pulse width, pulse frequency, and cutting speed. Their goal was to determine how these variables affected the kerf geometry and the metallurgical variation. Sharifi et al., [28]

conducted experimental research on the CO2 laser cutting of the material Al 6061 T6 alloy in order to investigate the impacts of laser process parameters such as speed, laser power, standoff distance, and sheet thickness on temperature and cutting-edge quality. It was discovered that the power of the laser has a significant impact on the output qualities that were examined. Anghel et al., [29] determine the impact of factors such as laser power, cutting speed, focal location, and gas pressure on efficiency feature of Surface roughness, operational research is conducted utilizing CO2 laser during the profile cutting of gears manufactured of alloy stainless steel 304. Elsheikh et al., [30] had carried out investigative research utilizing RSM in order to determine the impact of cutting variables such as cutting speed, gas pressure, laser beam power, and sheet thickness on cutting quality for said materials poly methyl methacrylate.

Producing complicated profiles using more conventional methods is a challenging task that takes a significant amount of time. In order to achieve the level of accuracy, it is necessary to adjust the laser process parameters to their optimal values. In this article an effort is made by using Box-Benhken design to determine the impact of varying laser process parameters on the size of the heat affected zone (HAZ) and the surface roughness (Ra). In this research paper, the effects of process parameters on the cut quality, heat-affected zone are observed.

2. METHODS AND MATERIALS

In this research, the material chosen was Hastelloy C-276 sheet or plate of the desired thickness and dimensions. Clean the surface of the material to remove any dirt, oil, or debris. Place the material on a flat and stable work surface.

Hastelloy C-276 is made up of 15.5% chromium, 0.6% magnesium, 0.088% carbon, 0.034% silicon, 0.001% Sulphur, and 0.004% phosphorus. In addition, it has 0.004% phosphorus and 0.001% Sulphur. The level of carbon, which has a range of values, is managed so that it is appropriate for almost all the service applications. The results of the Spectro analysis are presented in Table 1, which details the chemical composition of Hastelloy C-276; Table 2 meanwhile, details the mechanical properties of the materials that were utilized in the research [31].

Table 1. Chemical composition of Hastelloy C-276

Element	C	Mn	Si	S	P	Cr	Ni	Mo	Co	W	Fe	V
W%	0.005	0.41	0.02	0.002	0.005	15.83	Bal	16.36	0.05	3.45	6.06	0.17

Table 2. Carbon steel's mechanical characteristics

Material	Tensile strength (MPa)	Yield strength (MPa)	Elongation	Density
Hastelloy C-276	790	355	40%	8.89/cm3

Fig. 1 represents the laser cutting process of Hastelloy C-276 samples. The location of the focal plane in relation with the upper surface Hastelloy C-276 sheet having thickness of 3.7mm, is illustrated in the Fig. 2.

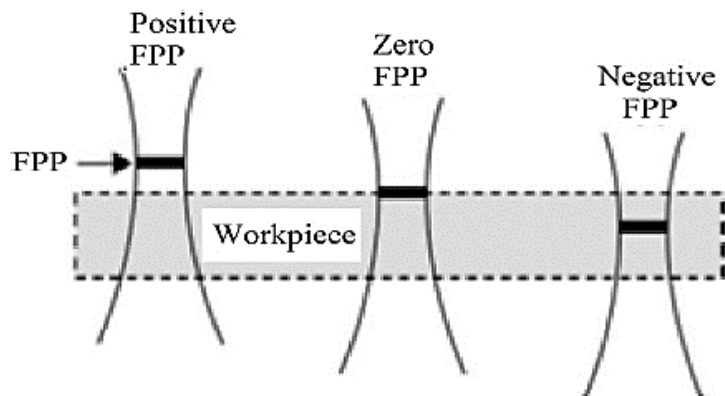Fig. 1. The laser cutting process of Hastelloy C-276 sheet

Fig. 2. The location of the focal plane in relation with the upper surface Hastelloy C-276 sheet

Laser system setup: For experimentation on the system a set up the laser cutting machine in a well-ventilated area with appropriate safety measures in place, including safety glasses, gloves, and a face mask is utilized. Before the experimentation it was ensured that the laser beam is properly aligned and focused. By using nitrogen as the assist gas, the cutting experiments are performed in a continuous 4 kW CO_2 laser cutting machine. Large number of trials were performed on the set up to determine the cutting parameters based on the thickness and composition of the Hastelloy material. These parameters include the laser power, cutting speed, and focal length of the lens. The parameters will depend on the specific laser cutting system being used and the desired cutting quality. Table 3 shows the input process parameter with their limiting range

Table 3. Input process parameter with limiting range

Input process parameters	Unit	Notation	Min Limit	Max Limit
Laser Power	Watt	LP	2400	3800
Cutting Speed	mm/min	CS	1100	2400
Gas Pressure	Bar	GP	11	17

3. DESIGN OF EXPERIMENTS

Box–Behnken designs, created in 1960 by George E. P. Box and Donald Behnken, are experimental designs for response surface methodology [32]. Each component, or independent variable, has one of three equally spaced values, commonly −1, 0, +1. (The following aim requires three levels.) The design should suit a quadratic model with squared terms, two-factor products, linear terms, and an intercept. The quadratic model's coefficient-to-experimental point ratio should be fair (in fact, their designs kept in the range of 1.5 to 2.6). The estimation variance should rely mostly on the distance from the center (this is achieved exactly for the designs with 4 and 7 components) and not change considerably inside the smallest (hyper) cube containing the experimental points. Rotatability Box-Behnken design outperforms three-level full factorial design, central composite design (CCD), and Doehlert design despite its weak corner coverage of nonlinear design space. Same kind of methodology was adopted by various researcher in the past for different processes and obtained the good results [33-39]. A specific number of factors are placed through all factorial design combinations in each block, while the remaining factors are retained at the center values. In the Box–Behnken design for three factors, three blocks vary two factors through the four potential high and low combinations. Include center points (in which all factors are at their central values). As per the stated design of experimental strategy the cutting parameters have been employed for the cutting and the experiments are performed on the Hastelloy material. During all the trials, the laser beam impact angle was kept at 900. A uniform distance was kept between the square profiles cut (20 mm × 20 mm × 3.7 mm), during each consecutive trial and in a single pass and a key-hole cut was also made in each specimen, for the purpose of measuring the kerf width.

In order to reduce the allowable range of process parameters and to sort out the acceptable upper and lower level of parameters. Under this experiment, complete cutting, the minimum value (surface roughness, Heat affected zone) were the governing aspects considered for determining the working ranges. The list of all parametric settings of rotatable   central composite designs, that are running along with their obtained corresponding responses are listed in the Table 4.
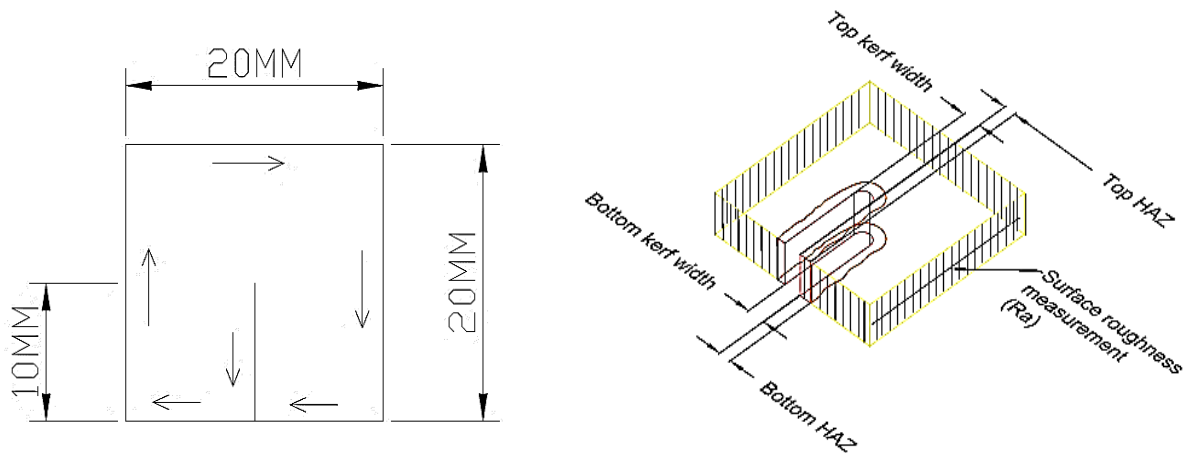
Fig. 3. Geometrical features of the cross-section of the kerf

Table 4. Experimental design matrix with the corresponding results for Hastelloy C276

Sr. No.	Laser power (watt)	Cutting speed (mm/min)	Gas pressure (bar)	HAZ (mm)	Surface roughness (µm)
1	3100	1762.5	14	0.190	0.95
2	3800	1762.5	17	0.196	1.17
3	3100	2400.0	11	0.199	1.02
4	3100	1762.5	14	0.191	0.96
5	3100	2400.0	17	0.188	0.99
6	3800	1762.5	11	0.191	1.16
7	3800	1125.0	14	0.209	1.15
8	2400	1125.0	14	0.153	0.89
9	2400	2400.0	14	0.136	0.77
10	2400	1762.5	17	0.123	0.86
11	3100	1125.0	11	0.214	1.08
12	3800	2400.0	14	0.196	1.10
13	3100	1762.5	14	0.190	0.96
14	2400	1762.5	11	0.148	0.88
15	3100	1125.0	17	0.201	1.09

After the cutting operation is complete, remove the Hastelloy material from the laser cutting machine. Inspect the cut for any rough edges, burrs, or other imperfections. Use appropriate post-processing methods to remove any imperfections and achieve the desired surface finish. Overall, laser cutting of Hastelloy requires careful attention to detail and adherence to safety protocols. By following the experimental strategy outlined above, one can achieve a clean and precise cut with minimal heat-affected zone.

3.1 Analysis of HAZ
Table 5. demonstrates the Box-Benhken design along with the "ANOVA" results for the obtained quadratic model of "HAZ." The "F-value" that was calculated for the model to be 1878.98, which indicates that the model is credible and reliable. This is because the F-value is a measure of the overall variation in the model which is explained by the term and the regressors. In addition to this, the model terms, and square terms for "laser power" (LP), "gas

pressure" (GP), and "cutting speed" (CS), were discovered. Table 5 shows the "F-value" foreach term, such as linear, squared, and interaction. A term with higher "F-value" would have a bigger effect on the model. The "laser power" has a "F-value" of 10623.10, which is higher than other parameters, indicating it has the most impact on "HAZ," followed by the "cutting speed" parameter and the "gas pressure" parameter. The value of "Pred R-Squared," which was found to be 99.61%, is in good agreement with the value of "Adj R-Squared," which was found to be 99.92%. These values are both measures of the model's goodness of fit, with R-squared representing the proportion of the variance in the dependent variable that can be explained by the independent variables. In addition, the P value for each of the parameters was found to be less than 0.05, indicating that the parameters are significantly contributing to the results obtained.

The Box-Benhken design is a powerful tool for finding the most impactful parameters for a given model. By using this design, it is possible to determine which parameters have the most significant effect on the model's outcome and to make decisions based on the results obtained. The F-value, R-squared and P-value are all indicators of the model's reliability and accuracy, which is essential in determining the best parameters for the model. In this case, the higher F-value and R-squared values indicate that the model is credible, and the lower P-value suggests that the parameters are contributing significantly to the results obtained. This provides insight into the parameters that have the most impact on "HAZ," and can be used to make data-driven decisions and optimize the model accordingly.

Table 5. ANOVA analysis of HAZ

Source	DF	Adj SS	Adj MS	F-Value	P-Value
Model	9	0.0107	0.0012	1878.98	0.00
Linear	3	0.0074	0.0025	3889.74	0.00
LP	1	0.0067	0.0067	10623.10	0.00
CS	1	0.0004	0.0004	663.95	0.00
GP	1	0.0002	0.0002	382.11	0.00
Square	3	0.0031	0.0010	1626.14	0.00
LP*LP	1	0.0026	0.0026	4068.38	0.00
CS*CS	1	0.0003	0.0003	535.43	0.00
GP*GP	1	0.0000	0.0000	1.98	0.22
2-Way	3	0.0002	0.0001	121.05	0.00
LP*CS	1	0.0000	0.0000	6.32	0.05
LP*GP	1	0.0002	0.0002	355.26	0.00
CS*GP	1	0.0000	0.0000	1.58	0.26
Error	5	0.0000	0.0000		
Lack-of-Fit	3	0.0000	0.0000	2.50	0.30
Pure Error	2	0.0000	0.0000		
Total	14	0.0107			
S: 0.0007958		R2: 99.97 %		R2(adj): 99.92%	R2(pred): 99.61 %

Regression equation for HAZ

HAZ = 0.1508+ 0.000322 LP-0.000105CS-0.01518 GP- 0.0 LP*LP+ 0.00 CS*CS+

0.000065GP*GP + 0.00 LP*CS + 0.000004 LP*GP+ 0.00 CS*GP ------------------- (1)

3.2 Analysis of Surface Roughness

The developed statistical model is tested by ANOVA, the results for the surface roughness are presented in Table 6. From this table the F value of 1251.81 suggests that the model is statistically important. also, since "Prob > F" is less than 0.05, the term containing factor effects such as "Laser Power" (LP), "Gas Pressure" (GP), and "Cutting speed" (mm/min) is important. Moreover, the obtained F value with possible probability i. e. P for all terms is presented in Table 4. Form this table it has been determined that the "F-value" of "laser power" is 9493.64, which is significantly greater than the values of the remaining variables. The "laser power" parameter is known to have the greatest influence on the "Surface roughness" metric, trailed by the "cutting speed" and "gas pressure" indices. Once again, the model's "Pred R-Squared" score of 99.61% demonstrates excellent concordance with the "Adj R-Squared" score of 99.88%.

Table 6. ANOVA analysis of surface roughness

Source	DF	Adj SS	Adj MS	F-Value	P-Value
Model	9	0.206548	0.022950	1251.81	0.000
Linear	3	0.187775	0.062592	3414.09	0.000
LP	1	0.174050	0.174050	9493.64	0.000
CS	1	0.013612	0.013612	742.50	0.000
GP	1	0.000112	0.000112	6.14	0.056
Square	3	0.016923	0.005641	307.70	0.000
LP*LP	1	0.000041	0.000041	2.24	0.195
CS*CP	1	0.002156	0.002156	117.62	0.000
GP*GP	1	0.015203	0.015203	829.23	0.000
2-Way	3	0.001850	0.000617	33.64	0.001
LP*CS	1	0.001225	0.001225	66.82	0.000
LP*GP	1	0.000225	0.000225	12.27	0.017
CS*GP	1	0.000400	0.000400	21.82	0.005
Error	5	0.000092	0.000018		
Lack-of-Fit	3	0.000025	0.000008	0.25	0.858
Pure Error	2	0.000067	0.000033		
Total	14	0.206640			
S: 0.0042817		R2: 99.96%		R2(adj): 99.88%	R2(pred): 99.73%

Regression equation for surface roughness

Ra = 2.192+ 0.000134 LP- 0.000323 CS - 0.20274GP - 0.0 LP*LP+ 0.0 CS*CS+
0.007130 GP*GP+ 0.00 LP*CS + 0.000004 LP*GP - 0.000005 CS *GP--------------(2)

4 RESULTS AND DISCUSSION

The influence of laser machining process parameters like "laser power", "cutting speed", "gas pressure", on "HAZ" and "surface roughness" is evaluated in detailed. The material is removed away because of the intense focused laser at the cutting zone. The results are discussed with the corresponding output characteristics as follows:

4.1 Heat affected zone (HAZ)

The effect that processes parameters, those used in laser machining, such as "laser power", "cutting speed", "gas pressure", on "HAZ" is shown as the main effects plots for "HAZ" in Fig. 4. Throughout the laser cutting of Hastelloy C-276, it is impossible to prevent seeing "HAZ." As the amount of "laser power" goes up, the performance feature "HAZ" goes up gradually. This occurs since the value of "laser power" grows, its intensity on the workpiece material for machining also increases, which results in a degradation of the side upper face of the cutting zone as illustrated in Fig. 4. To reduce how much "laser power" affects "HAZ," a minimum number is preferable. It is observed from Fig. 5 that as the value of "cutting speed" increases, the performance characteristics "HAZ" decreases. As the value of "cutting speed" increases, it reduces the time for machining and interaction of "laser power" with the workpiece material results in desirable HAZ.

It is observed from the Fig. 6-8 as the "gas pressure" increases; there is a gradual decrease in the performance characteristics "HAZ". Whenever the value of "gas pressure" increases, the focused of the beam is more confine towards the cut results in reduction of "HAZ". Further, "gas pressure" gives to the cooling of the workpiece and therefore, greater values of gas pressure contribute towards reduction in the amount of the surrounding "HAZ". It is concluded that the minimum "HAZ" would occurs at lower values of "laser power" and higher value of "cutting speed".
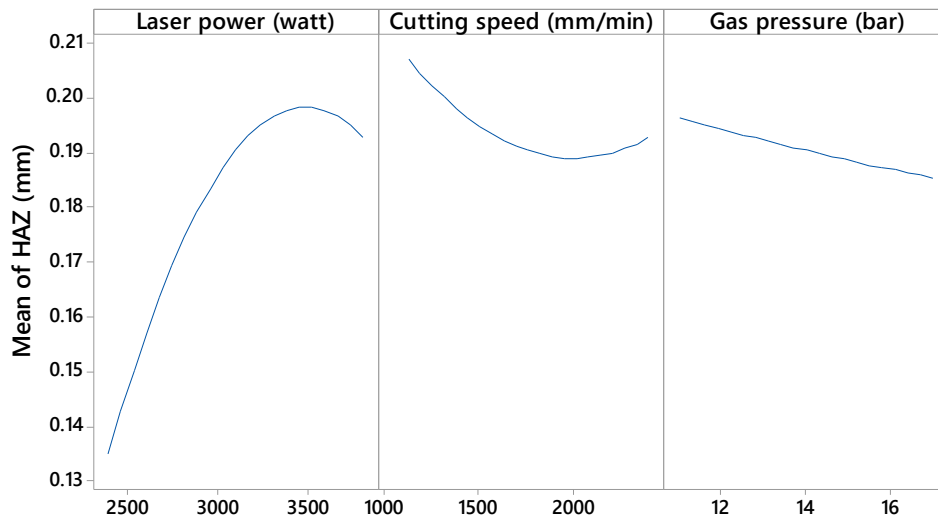

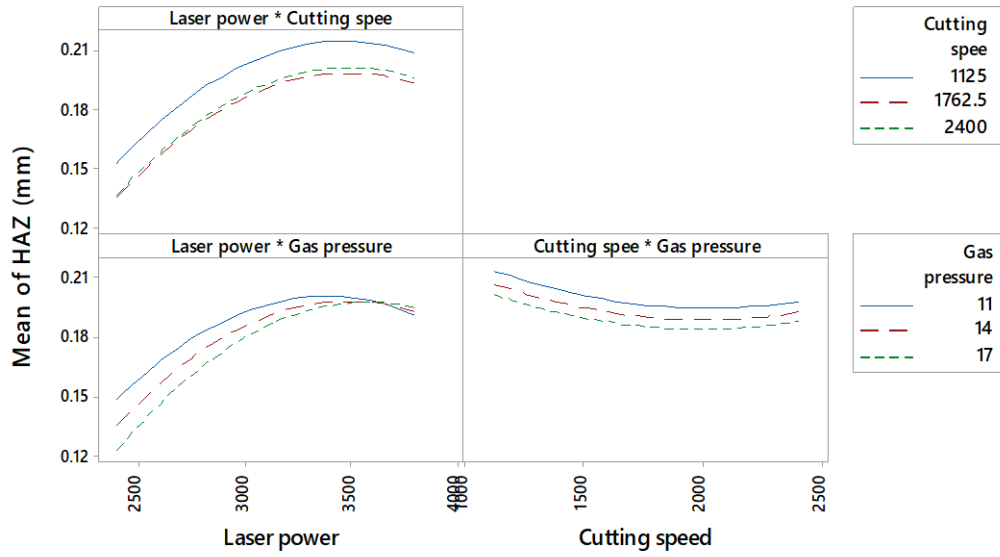Fig. 4. Main effects plots of HAZ

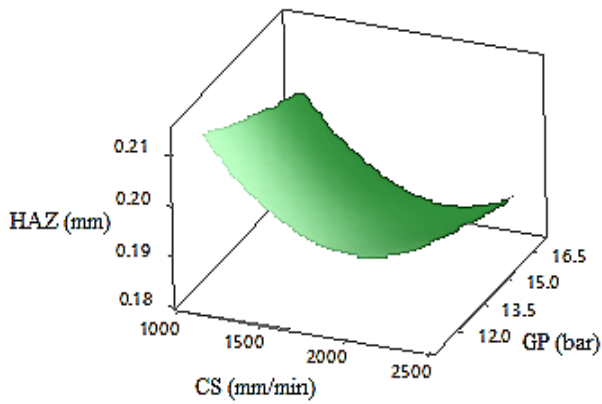Fig. 5. Interaction plots of HAZ

Fig. 6. Surface plot of HAZ vs GP, CS
hold values LP

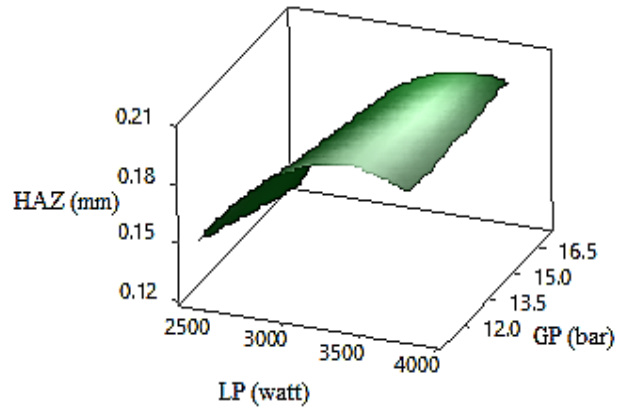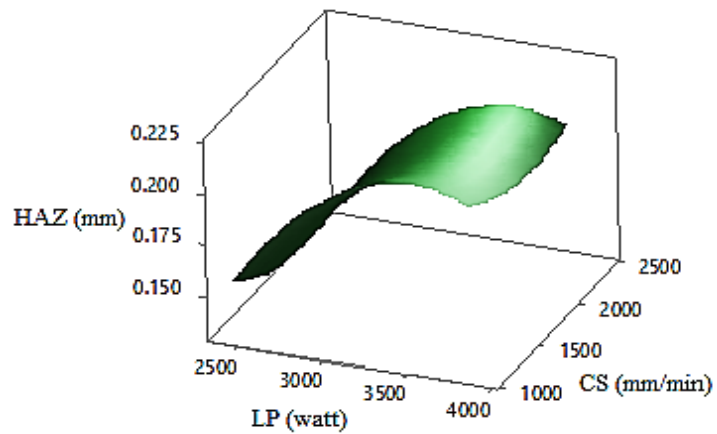Fig. 7. Surface plot of HAZ vs GP, LP
hold values CS

Fig. 8. Surface plot of HAZ vs CS, LP hold values GP

4.2 Surface Roughness (Ra)

The main effect of selected laser machining parameters like "laser power", "cutting speed", "gas pressure" on "Ra" is shown in Fig. 9. As the value of "laser power" increases the performance characteristic "Ra" is degrading rapidly. This occurs because as the value of "laser power" increases, its strength on the workpiece material for machining increases which degrades the side face of the specimen. To reduce the effect "laser power" on "Ra" minimum value is desirable. It is observed from Fig. 10 as the value of "gas pressure" increases; the performance characteristics "Ra" improved gradually. This is because as the value of gas pressure increases it creates thrust at side face along with "laser power" which produces intense energy to cut the specimen smoothly.
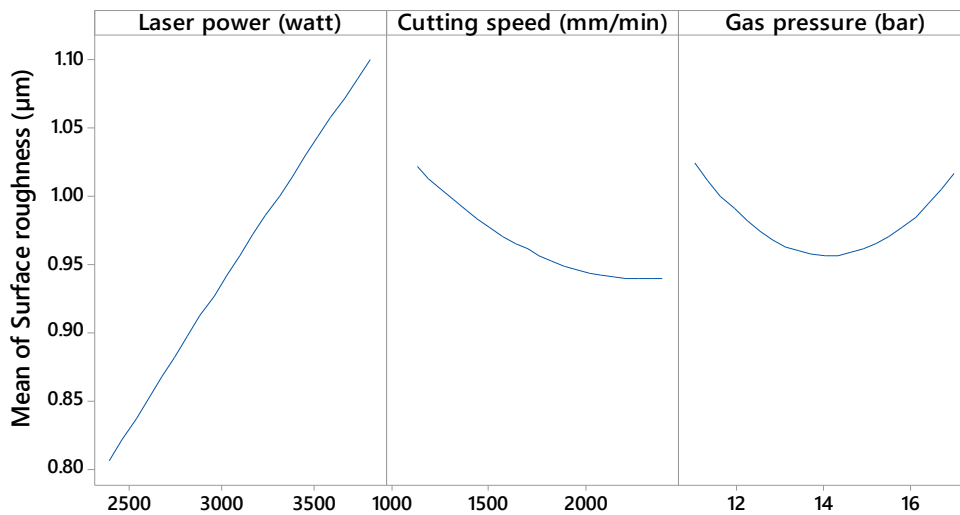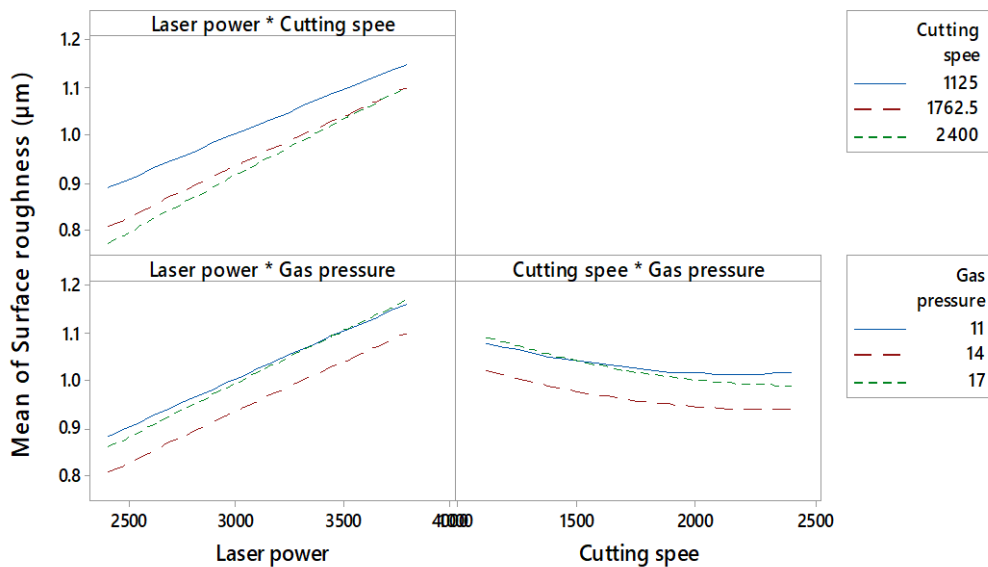

Fig. 9. Main effects plots of Surface roughness

Fig. 10. Interaction plots of Surface roughness

The effect of selected laser machining parameters like "laser power", "cutting speed", "gas pressure" on "Ra" is shown in Fig.11-13. As the value of "laser power" increases the performance characteristic "Ra" is degraded rapidly. This occurs because as the value of "laser power" increases, its strength on the workpiece material for machining increases which degrades the side face of the specimen. To reduce the effect "laser power" on "Ra" minimum value is desirable. It is observed from response plots, as the value of "gas pressure" increases; the performance characteristics "Ra" improved gradually (little effect). This is because as the value of gas pressure increases it creates thrust at side face along with "laser power" which produces intense energy to cut the specimen smoothly.
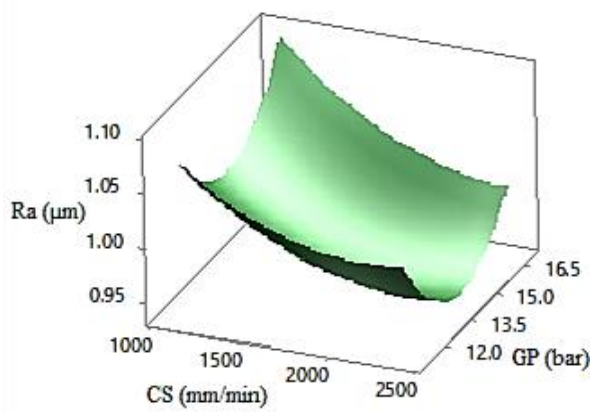

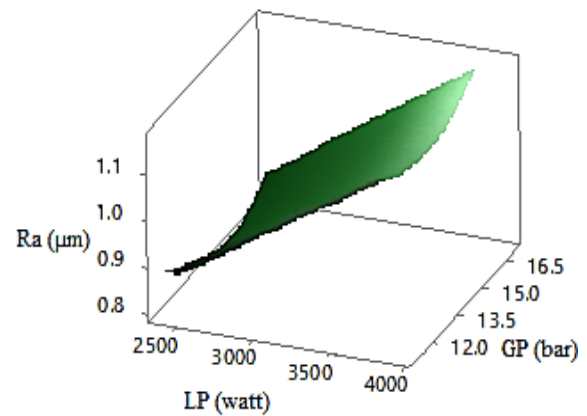Fig. 11. Surface plot of Ra vs GP, CS
hold values LP

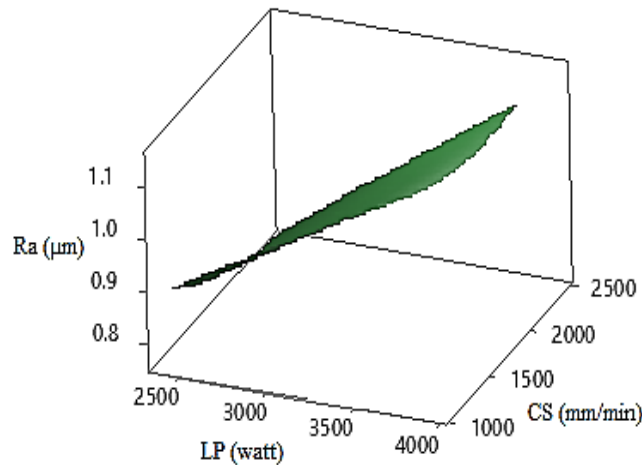Fig. 12. Surface plot of Ra vs GP, LP
hold values CS

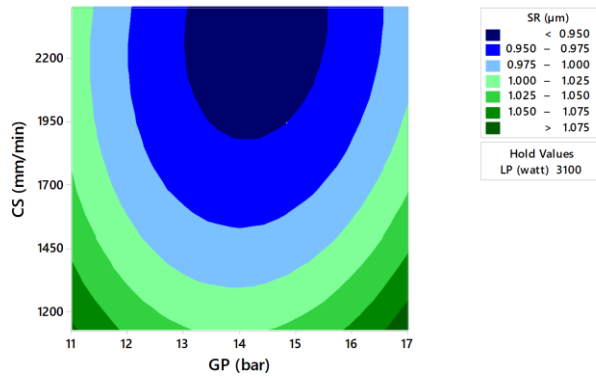Fig. 13. Surface plot of Ra vs CS, LP hold values GP

Fig. 14. Contour plot of CS vs GP,
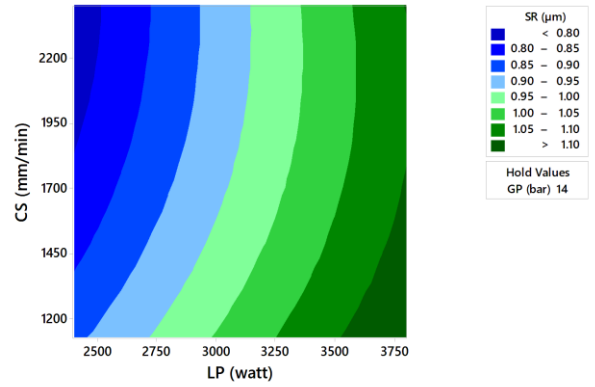hold values LP

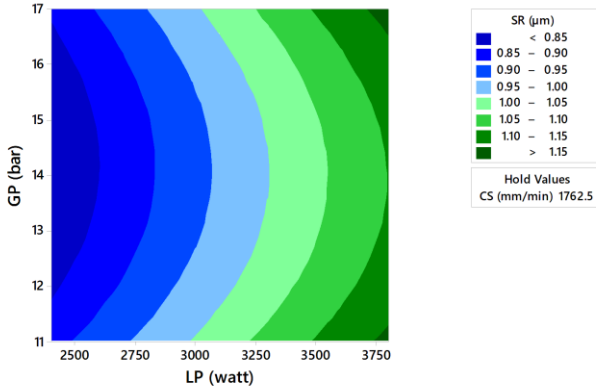Fig. 15. Contour plot of Ra vs CS,
hold values LP

Fig. 16. Contour plot of GP vs LP,
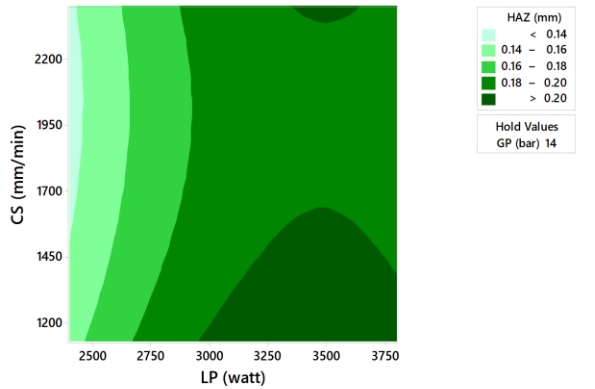hold values CS

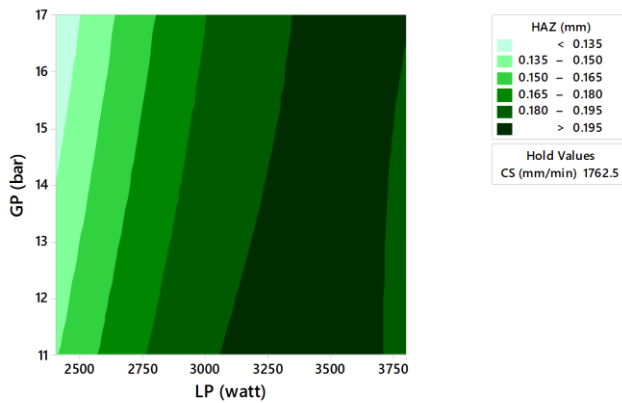

Fig. 17. Contour plot of CS vs LP,
hold values GP

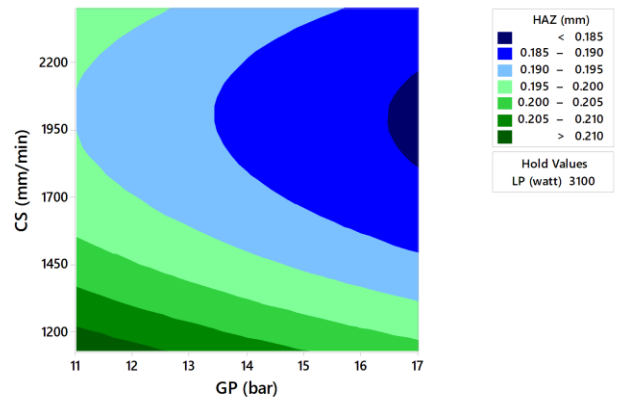Fig. 18. Contour plot of GP vs LP,
hold values CS

Fig. 19. Contour plot of CS vs GP,
hold values LP

4.3 Optimization and confirmation test

The results of using the Box-Behnken design approach with response surface methodology (RSM) to optimize laser machining process parameters for the material Hastelloy C-276 sheet revealed that when using the optimal combination of parameters, including a laser power of 2400 watts, gas pressure of 15.66 bar, and cutting speed of 2232.58 mm/min, yielded an increase in the performance and quality of the machined parts. Specifically, this combination yielded a surface roughness of 0.78 (µm), a heat-affected zone (HAZ) of 0.127 mm. These results demonstrate that this combination of parameters is the optimal choice for achieving the highest performance and quality of the machined parts. Furthermore, the results reveal that the laser power has the greatest influence on the performance and quality of the machined parts, followed by the feed rate and the scanning speed. Therefore, it is important to adjust the laser power to the optimal value in order to achieve the best results.

Overall, the Box-Behnken design approach with response surface methodology (RSM) is a powerful tool that can be used to optimize laser machining process parameters for the material Hastelloy C-276 sheet. With this approach, the process parameters can be adjusted to yield the desired performance and quality of the machined parts. Table 7 shows the predicted and actual results of optimized parameter where obtained result shows good agreement with the predicted results.

Table 7. Predicted and actual results of optimized parameter

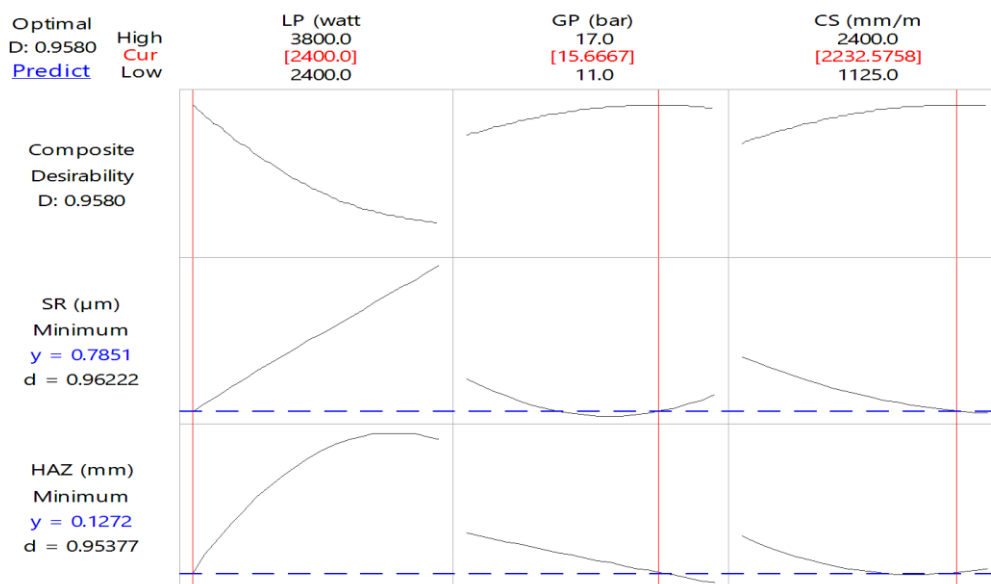| Sr. No.	Parameter	Level	Predicted results	Actual results	% error
1	LP (watt)	2400	Ra = 0.78 (µm)	Ra = 0.80 (µm)	2.56
2	GP (bar)	15			
3	CS (mm/min)	2232	HAZ = 0.127 (mm)	HAZ = 0.135 (mm)	6.29

Fig. 20. Optimization plot

5. CONCLUSIONS

In this study, the laser machining process parameters for the material Hastelloy C-276 sheet are improved with the help of Box Benhken design approach with response surface methodology. This approach is used to determine the most optimal values for the parameters. The primary goal of this investigations is to optimize the output characteristics, which include "HAZ" and "Ra" for the selected range of process parameters which include "laser power," "cutting speed," "gas pressure," The major conclusions of this research are that the Box-Behnken design approach with response surface methodology (RSM) is a powerful tool that can be used to optimize laser machining process parameters for the material Hastelloy C-276 sheet in order to achieve the desired performance and quality of the machined parts.

1. "Laser power" is found to be the most significant factor in determining Ra and HAZ.

2. Using the many process factors that are taken into consideration, regression models are created for "HAZ," "Ra," These regression models are optimized in order to acquire the best possible value of the process parameters that are being considered for the laser machining process.

3. Specifically, the optimal combination of parameters yielded an increase in performance and quality of the machined parts with a surface roughness of 0.78 (µm) and HAZ of 0.12 mm.

4. Furthermore, it was determined that the laser power has the greatest influence on the performance and quality of the machined parts, followed by the feed rate and the cutting speed, thus emphasizing the importance of setting the laser power to the optimal value.

5. The research also showed that the optimal combination of parameters for laser machining of Hastelloy C276 included a laser power of 2400 watts, gas pressure of 15.66 bar, and cutting speed of 2232.58 mm/min.

6. This demonstrates that the Box-Behnken design approach with response surface methodology (RSM) can maximize the performance and quality of the machined parts by adjusting the process parameters to the optimal values. Additionally, the results of this study demonstrate the importance of setting the laser power to the optimal value in order to achieve the best results.

7. Additionally, the results of this study demonstrate that the Box-Behnken design approach with response surface methodology (RSM) can be used to optimize laser machining process parameters for the material Hastelloy C-276 sheet in order to achieve the desired performance and quality of the machined parts.

REFERENCES

[1] Hashim, M., Sarath Raghavendra Babu, K., Duraiselvam, M., & Natu, H. (2013). Improvement of wear resistance of Hastelloy C-276 through laser surface melting. Materials& Design (1980-2015), 46, 546-551.

[2] Ma, G., Wu, D., Niu, F., & Zou, H. (2015). Microstructure Evolution and mechanical property of pulsed laser welded NI-based superalloy. Optics and Lasers in Engineering, 72, 39- 46.

[3] Senthilkumar, V., Adinarayanan, A., & Jagatheesan, K. (2023). Grey relational analysis (GRA) for optimization of CO2 laser cutting of Stainless Steel. Materials Today: Proceedings, 72, 2437-2442.

[4] Hiwale, S., & Rajiv, B. (2021). Experimental investigations of laser machining process parameters using response surface methodology. Materials Today: Proceedings, 44, 3939-3945.

[5] Madic, M., Petrovic, G., Petkovic, D., Antucheviciene, J., & Marinkovic, D. (2022). Application of a robust decision-making rule for comprehensive assessment of laser cutting conditions and performance. Machines, 10(2), 153.

[6] Dubey, A. K., & Yadava, V. (2008). Laser Beam Machining—A Review. International Journal of Machine Tools and Manufacture, 48(6), 609-628.

[7] Patidar, D., & Rana, R. (2018). The effect of CO2 Laser Cutting parameter on mechanical & microstructural characteristics of high strength steel-A Review. Materials Today: Proceedings, 5(9), 17753-17762.

[8] Shrivastava, P. K., & Pandey, A. K. (2018). Parametric optimization of multiple quality characteristics in laser cutting of Inconel-718 by using hybrid approach of multiple regression analysis and genetic algorithm. Infrared Physics & Technology, 91, 220-232.

[9] Sharma, A., & Yadava, V. (2018). Experimental Analysis of ND-YAG laser cutting of sheet materials – a review. Optics & Laser Technology, 98, 264-280.

[10] Yongbin, Y., Bagherzadeh, S. A., Azimy, H., Akbari, M., & Karimipour, A. (2020). Comparison of the artificial neural network model prediction and the experimental results for cutting region temperature and surface roughness in laser cutting of AL6061T6 alloy. Infrared Physics & Technology, 108, 103364.

[11] Santosh, S., Kevin Thomas, J., Pavithran, M., Nithyanandh, G., & Ashwath, J. (2022). An experimental analysis on the influence of CO2 laser machining parameters on a copper-based shape memory alloy. Optics & Laser Technology, 153, 108210.

[12] Madic, M., Antucheviciene, J., Radovanovic, M., & Petković, D. (2017). Determination of laser cutting process conditions using the preference selection index method. Optics & Laser Technology, 89, 214-220.

[13] Gnanavelbabu, A., Arunachalam, V., Sunu Surendran, K. T., Rajkumar, K., & Anandhababu, E. (2020). Optimization of CO2 laser cutting parameters for AA6061/B4C/HBN Hybrid Composites using Taguchi-based response surface methodology. Lecture Notes in Mechanical Engineering, 111–122.

[14] Girdu, C. C., & Gheorghe, C. (2022). Energy efficiency in CO2 laser processing of Hardox 400 material. Materials, 15(13), 4505.

[15] Hiwale, S., & Rajiv, B. (2021). Experimental investigations of laser machining process parameters using response surface methodology. Materials Today: Proceedings, 44, 3939–3945.

[16] Wang, J., Sun, Z., Gu, L., & Azimy, H. (2021). Investigating the effect of laser cutting parameters on the cut quality of Inconel 625 using Response surface method (RSM). Infrared Physics & Technology, 118, 103866.

[17] Santosh, S., Kevin Thomas, J., Pavithran, M., Nithyanandh, G., & Ashwath, J. (2022). An experimental analysis on the influence of CO2 laser machining parameters on a copper-based shape memory alloy. Optics & Laser Technology, 153, 108210.

[18] Naresh, & Khatak, P. (2022). Laser cutting technique: A literature review. Materials Today:Proceedings, 56, 2484–2489.

[19] Zeilmann, R. P., & Conrado, R. D. (2022). Effects of cutting power, speed and assist gas pressure parameters on the surface integrity cut by laser. Procedia CIRP, 108, 367–371.

[20] Hashim, M., Sarath Raghavendra Babu, K. E., Duraiselvam, M., & Natu, H. (2013). Improvement of wear resistance of Hastelloy C-276 through laser surface melting. Materials& Design (1980-2015), 46, 546–551.

[21] Hasçalık, A., & Ay, M. (2013). CO2 laser cut quality of Inconel 718 nickel – based superalloy. Optics & Laser Technology, 48, 554–564.

[22] Madic, M., Antucheviciene, J., Radovanovic, M., & Petkovic, D. (2017). Determination of laser cutting process conditions using the preference selection index method. Optics & Laser Technology, 89, 214–220.

[23] Moradi, M., Mehrabi, O., Azdast, T., & Benyounis, K. Y. (2017). Enhancement of low power CO2 laser cutting process for injection molded polycarbonate. Optics & Laser Technology, 96, 208–218.

[24] Shrivastava, P.K. and Pandey, A. K. (2018). Parametric optimization of multiple quality characteristics in laser cutting of inconel-718 by using hybrid approach of multiple regression analysis and genetic algorithm. Infrared Phy. Technol. 91, 220- 232.

[25] Kotadiya, D.J., Kapopara, J.M., Patel, A.R., Dalwadi, C.G. Pandya, D.H. (2018). Parametric analysis of process parameter for Laser cutting process on SS-304. Mater. Today: Proceed. 5, 5384– 5390.

[26] Stournaras, A., Stavropoulos, P., Salonitis, K. and Chryssolouris, G. (2009). An investigation of quality in CO2 laser cutting of aluminum. CIRP J. Manuf. Sci. Technol. 2 61– 69.

[27] Joshi, P. and Sharma, A. (2018). Simultaneous optimization of kerf taper and heat affected zone in Nd-YAG laser cutting of Al 6061-T6 sheet using hybrid approach of grey relational analysis and fuzzy logic. Prec. Engi. 54, 302 – 313.

[28] Sharifi, M. and Akbari, M. (2019). Experimental investigation of the effect of process parameters on cutting region temperature and cutting-edge quality in laser cutting of AL6061T6 alloy. Optik Int. J. Light Elec. 184, 457–463.

[29] Anghel, C., Gupta, K. and Jen, T.C. (2019). Analysis and optimization of surface quality of stainless-steel miniature gears manufactured by CO2 Laser cutting. Optik. 203, 164049.

[30] Elsheikh, A.H., Deng, W. and Showaib, E.A. (2019). Improving laser cutting quality of polymethyl methacrylate sheet: experimental investigation and optimization. J. Mater. Res. Technol. (Article in press).

[31] Manikandan, M., Hari, P. R., Vishnu, G., Arivarasu, M., Ramkumar, K. D., Arivazhagan, N., Rao, M. N., & Reddy, G. M. (2014). Investigation of microstructure and mechanical properties of super alloy C-276 by continuous nd: YAG laser welding. Procedia Materials Science, 5, 2233–2241.

[32] Ferreira, S. L. C., Bruns, R. E., Ferreira, H. S., Matos, G. D., David, J. M., Brandão, G. C., da Silva, E. G. P., Portugal, L. A., dos Reis, P. S., Souza, A. S., & dos Santos, W. N. L. (2007). Box-Behnken Design: An alternative for the optimization of Analytical Methods. Analytica Chimica Acta, 597(2), 179–186.

[33] Deshmukh, D. D., and V. D. Kalyankar (2019) "Deposition Characteristics of Multitrack Overlay by Plasma Transferred Arc Welding on SS316Lwith Co-Cr Based Alloy– Influence of Process Parameters." High Temperature Materials and Processes 38, 248- 263.

[34] Kakade, S. P., A. G. Thakur, D. D. Deshmukh, and S. B. Patil (2022) "Experimental investigations and optimisation of Ni-Cr-B-Si hardfacing characteristics deposited by PTAW process on SS 410 using response surface method" Advances in Materials and Processing Technologies 1-17.

[35] Deshmukh, D. D., and V. D. Kalyankar (2018) "Recent status of overlay by plasma transferred arc welding technique." International Journal of Materials and Product Technology 56 (1-2) 23-83.

[36] Naik, H. V., D. D. Deshmukh, and V. D. Kalyankar (2022) "Study of Heat Treatment Effecton Microstructure of PTA Weld Deposited Surface of SS 316L Steel."

[37] Deshmukh, D. D., and V. D. Kalyankar (2021) "Analysis of deposition efficiency and distortion during multitrack overlay by plasma transferred arc welding of Co–Cr alloy on 316L stainless steel." Journal of Advanced Manufacturing Systems 20 (04),705-728.

[38] Deshmukh, D. D., and V. D. Kalyankar (2019) "Evaluation of surface characteristics of PTAW Hardfacing based on energy and powder supplied." In Advances in Micro and Nano Manufacturing and Surface Engineering: Proceedings of AIMTDR 2018, pp. 547-558. Singapore: Springer Singapore, 2019.

[39] Kalyankar, V. D., and D. D. Deshmukh (2017) "Failure investigations of failed valve plug SS410 steel due to cracking." In IOP Conference Series: Materials Science and Engineering, 282 (1) p. 012007.

BACK

EXPERIMENTAL ANALYSIS ON LASER CUTTING OF HASTELLOY C 276: EFFECTS OF PROCESS PARAMETERS ON KERF WIDTH, SURFACE ROUGHNESS, HAZ USING TAGUCHI TECHNIQUE

Sagarkumar J. Aswar[1], Nilesh Diwakar[2], Shyamkumar D. Kalpande[3]

[1]Ph.D. Research Scholar, RKDFIST, SRK University, Bhopal, India.
[2]Prof., Department of Mechanical Engineering, RKDFIST, SRK University, Bhopal, India.
[3]Prof., Department of Mechanical Engineering, GCOERC, Nashik, India.

Corresponding author: Sagarkumar J. Aswar, sagaraswar123@gmail.com

Abstract

Hastelloy C276, a nickel-based alloy widely utilized in aerospace, defense, energy, and food processing, was the subject of an experimental investigation presented here in order to determine the optimal laser machining process parameters for this material. In laser cutting, a high-powered laser beam melts and vaporizes the material without ever touching it. The effects of laser machining process parameters (laser power, cutting speed, and gas pressure) on Kerf width, surface roughness (Ra), Heat-Affected Zone (HAZ) were studied using the Taguchi method experimental design with the analysis of variance (ANOVA) methodology. Which measurement is the most precise is determined using the signal to noise ratio. Using certain optimization techniques, a set of parameters that are close to the best ones was constructed to achieve the good results.

Keywords: Heat-Affected Zone (HAZ), surface roughness (Ra), Kerf Width, Hastelloy C-276, cutting speed, laser power, gas pressure, Taguchi Method,

1. INTRODUCTION

Hastelloy is a group of nickel-based alloys with excellent strength, corrosion resistance, and heat resistance due to the addition of molybdenum, chromium, and other metals in various proportions. Because of its durability and resistance to corrosion, Hastelloy is frequently used in industries like chemical processing, oil and gas production, defense, and aerospace. It has also been a very desirable material for use in maritime situations [1-3]. Since it can cut many different materials quickly and precisely, laser cutting has become increasingly popular in recent years. Due to its high melting point, limited thermal conductivity, and tendency to form a hard and brittle heat-affected zone (HAZ) during laser cutting, Hastelloy presents unique challenges [4-5]. In this investigation, the state of laser cutting technology for Hastelloy and discuss its possible uses across a range of sectors. When it comes to cutting Hastelloy, laser cutting has several advantages over more conventional methods like plasma or water jet cutting [6-7].

To begin, laser cutting is a type of cutting that does not involve any physical contact and does not call for the use of any sort of mechanical force, which lowers the possibility of the material being damaged. Second, laser cutting results in a thin kerf width as well as a smaller heat affected zone (HAZ). These characteristics contribute to the reduction of production waste and

damage. Finally, laser cutting can reach high cutting speeds and maintaining high levels of accuracy, which makes it a perfect option for applications involving mass manufacturing and complex structures [8-11]. Yet, there are several restrictions when it comes to cutting Hastelloy using a laser. The tremendous amount of energy that is being input by the laser beam has the possibility of causing the material to melts, vaporize, and oxidized, which can result in surface roughness, cracking, and porosity [12-14]. In additional to this, the thermal stress that is generated by the laser beam may leave the material with a distorted appearance and an increased level of residual stress. When cutting Hastelloy with a laser, the accuracy of the cut is determined by several different process parameters, including the laser power, cutting speed, focal location, assist gas, and nozzle diameter. Cutting depths, kerf width, and edge roughness are all affected by the amount of energy given by the laser [15-16]. The cutting speed influences the amount of heat that is transferred into the material as well as the time at which it cools, which also influences the material's microstructure and HAZ thickness. The spot size and energy density at the cutting surface are both affected by the focal location because it is affecting the focus diameter and structure of a laser beam. The assist gas, frequently composed of nitrogen or oxygen, works to evacuate the molten material, and prevent oxidation in the cutting zone [17-19]. The gas flow rate and pressure are affected by the size of the nozzle, which changes the gas flow pattern and the shape of the molten pool. Laser surface treatment in an argon atmosphere was used to improve the wear resistance of Hastelloy C-276.

This is where consumers found the best laser parameter settings for making a wear-resistant surface without making a brittle phase [20-21]. Researchers looked at how certain laser cutting process parameters affect Ra and HAZ when Inconel 718, a nickel-based super alloy, is machined. Using an X-ray and a scanning electron microscope. aimed to utilize the preference selection index technique to identify the optimal values for the CO2 laser cutting process parameters that enhance the target qualities during machining of stainless steel (Ra, HAZ, kerf width, and MRR). laser process factors including laser power, cutting speed, and focal position were analyzed statistically using the RSM method to determine their effect on the characteristics "Ra and geometry" when cutting polycarbonate sheets. Using a compressed gas and a Nd:YAG laser, one can achieve a high-frequency cut, The kerf deviation, kerf breadth, and kerf taper were all represented in a multi-objective optimization [22–24]. Particle swarm optimization, a swarm-based optimization method, was used to maximize the objective function, i.e., the geometrical quality, of an experiment conducted on Inconel-718 using a pulsed Nd:YAG laser beam [25]. Analyze the effect of variables including laser intensity, cutting speed, focus point, and gas pressure, when cutting the profile of gears made of alloy stainless steel 304, surface roughness and operational studies are undertaken using a CO2 laser [26]. Investigation research using RSM to examine the effect of cutting variables such as cutting speed, gas pressure, laser beam power, and sheet thickness on the cutting quality of poly methyl methacrylate materials [27]. Experimental studies on the effects of speed, laser power, standoff distance, and sheet thickness on temperature and cutting-edge quality during CO2 laser cutting of Al 6061 T6 alloy. It was found that the evaluated output quality is significantly affected by the power of the laser [28].

The quality of the cut made on Hastelloy C 276 is the highest importance, hence the primary purpose of this study is to investigate the parameters that influence the cutting process on specific machines. Therefore, in order to construct the experimentation, a Taguchi L_9 and an

orthogonal array was utilized to find the ideal settings for the laser cutter so that the Kerf width, average surface roughness, and HAZ of the cutting material can be kept to a minimum in the most efficient conditions for Hastelloy C 276. This will allow for the most accurate cutting possible. A study has investigated how the three major process parameters like laser power, cutting speed, and gas pressure have an impact on the kerf width, average surface roughness, and the HAZ during a process.

2. METHODS AND MATERIALS

2.1 Taguchi Method

Genichi Taguchi created a set of mathematical techniques sometimes referred to as "robust design methods" to enhance the quality of manufactured items; these techniques have since found applications in engineering, biology, advertising, and more [29-32]. Expert statisticians have praised Taguchi's efforts and the results they've produced, especially his work in developing designs for analyzing variance, but they've also pointed out the ineffectiveness of several of Taguchi's recommendations [33-34].

2.1.1 Loss functions in the statistical theory

In the past, treatment effects were estimated using mean-unbiased estimators in statistical models. Least squares estimators have the smallest variance of any mean-unbiased linear estimators under the assumptions of the Gauss-Markov theorem. The law of large numbers, which states that sample means converge to the true mean, also provides comfort for the prevalent use of mean comparisons. In his experimental design textbook, Fisher stressed the importance of comparing treatment means. however, loss functions were avoided by Ronald A. Fisher [35].

2.1.2 Taguchi's use of loss functions

Taguchi's knowledge of statistical theory came primarily from those who, like Ronald A. Fisher, shied away from loss functions. Taguchi, responding to Fisher's approach to experimental design, saw in it an opportunity to improve the average results of a process. Indeed, long-term programs to improve harvests were a major inspiration for Fisher's work, specifically programs to compare agricultural yields under different treatments and blocks.

However, Taguchi realized that in much industrial production, there is a need to produce an outcome on target, for example, to machine a hole to a specified diameter, or to manufacture a cell to produce a given voltage. He also realized, as had Walter A. Shewhart and others before him, that excessive variation lay at the root of poor manufactured quality and that reacting to individual items inside and outside specification was counterproductive.

Therefore, he argued, quality engineering must first consider the costs associated with poor quality in a variety of contexts. Quality costs are often calculated as the number of products that are out of specification times the price per unit for rework or scrap in traditional industrial engineering. Taguchi, on the other hand, pushed for manufacturers to widen their perspectives to include societal cost. Any manufactured item that deviates from nominal will incur some loss to the customer or the larger community, whether it be through premature wear and tear, difficulties in interfacing with other parts (which are also likely to deviate widely from nominal), or the need to build in safety margins. Manufacturers tend to disregard these costs

because they have little bearing on their bottom line and are instead concerned with their own. Analyses of public economics show that these externalities hamper the effective functioning of markets.

Taguchi claimed that if manufacturers took steps to reduce such losses, it would improve their brand's reputation, help them gain market share, and ultimately increase revenues. This would be comparable to the tragedy of the commons.

When an item is extremely minute, any losses are minimal. Within the bounds of the specifications, we can ignore the possibility of losses, as Donald J. Wheeler put it. Losses increase when we deviate from nominal, and we reach the specification limit when the losses are no longer ignorable. Taguchi sought a statistically meaningful way to reflect these losses, which W. Edwards Deming would characterize as "unknown and unknowable". Taguchi outlined three cases in which [36]

- Larger the better (for example, agricultural yield),
- Smaller the better (for example, carbon dioxide emissions),
- On-target, minimum-variation (for example, a mating part in an assembly).

In this context, the Taguchi method was used to establish the optimal values for the processing variables that would result in the lowest kerf width, Surface roughness and HAZ during the CO2 Laser cutting. Taguchi suggested adopting orthogonal arrays to collect unique information and analyzing the information to discover the optimal approach variables. The Taguchi quality concept design suggests that there are three possible output features to consider when evaluating the signal-to-noise ratio: the lower-the-better, the higher-the-better, and the nominal-the-better. Using orthogonal arrays, this approach requires only a small sample size to evaluate a wide variety of parameters. There is a correlation between a higher signal-to-noise ratio and improved output characteristics. In this case, the best S/N ratio performance can be achieved at the stage of the process parameters. The lower kerf width, Surface roughness and HAZ have been chosen for the characteristics that will maximize machining productivity. The measurements of output period were used in the following equation to determine the values for the lower is better criterion for the corresponding S/N ratios.

$$\text{S/N ratio } (\eta) = -10\log_{10}\frac{1}{n}\sum_{i=1}^{n} y_i{}^2$$

2.2 Material

Hastelloy C-276 with 3.7 mm sheet was selected as the material for this investigation. Hastelloy C-276 is split into its essential chemicals and presented in Table 1. The preparation of the material, a sheet made of Hastelloy that has the required thickness and dimensions. It is important to clean the surface of the material so that any dirt, grease, or debris can be removed. Put the materials down on a work area that is stable and level. Hastelloy C 276 has 15.5% chromium, 0.6% magnesium, 0.088% carbon, 0.034% silicon, 0.001% Sulphur, and 0.004% phosphorus. Carbon level, which has a mixed value, is kept at a level that is good for most service uses. After Spectro analysis, Table 1 shows the chemical composition of the sample, and Table 2 shows how the materials used in the research worked.

Table 1. Chemical composition of Hastelloy C-276

Element	C	Mn	Si	S	P	Cr	Ni	Mo	Co	W	Fe	V
W%	0.005	0.41	0.02	0.002	0.005	15.83	Bal	16.36	0.05	3.45	6.06	0.17

Table 2. Carbon steel's mechanical characteristics

Material	Tensile strength (MPa)	Yield strength (MPa)	Elongation	Density
Hastelloy C-276	790	355	40%	8.89/cm3

2.2.1 Experimental setup

The laser cutting machine is set up as shown in Fig 1 which is continuous 4 kW CO2 laser cutting machine. This machine set up was utilized for the said investigations, where it is kept in a well-ventilated area. The cutting operations were performed with safety glasses, gloves, and a face mask. Before the experiment, the laser beam was checked to make sure it was aligned and focused correctly by performing the trail experimentations in a Nitrogen assist gas.

Fig. 1. Experimental set up of laser cutting process

3. PROCESS PARAMETERS AND DESIGN OF TESTS (DOE)

Research can carry out more methodically by using the Design of Experiments. The process factors and their respective levels are presented in Table 3. When analyzing a wide variety of parameter options, the Taguchi technique employs a straightforward layout of orthogonal arrays and a limited number of test cycles. The research utilized a Taguchi-based experimental setup with a typical L_9 orthogonal array and three levels of three essential process parameters, such as laser power, cutting speed, and gas pressure.

Table 3. Process Factors and Levels

Input process	Unit	Notation	Min Limit	Max
Laser Power	watt	LP	2100	3500
Cutting Speed	mm/min	CS	1200	2500
Gas Pressure	bar	GP	12	16

L_9 orthogonal arrays are used to estimate a high number of critical effects in a perpendicular way with a small sample size. These arrays are also used to set up experiments that use a L_9 orthogonal matrix. Table 4, shows DOE with the obtained surface roughness, kerf width, HAZ and S/N ratio for each experimental condition

Table 4. DOE with the obtained surface roughness, kerf width, HAZ and S/N ratio

Exp. No.	LP	CS	GP	Ratio of kerf width	SNRA1	Surface Roughness	SNRA2	HAZ	SNRA3
1	2100	1200	12	1.17	2.64	0.84	1.51	0.16	15.91
2	2100	1850	14	1.91	-1.48	0.74	2.61	0.14	17.07
3	2100	2500	16	0.85	4.84	0.70	3.09	0.12	18.41
4	2800	1200	14	1.49	-0.45	0.95	0.44	0.19	14.42
5	2800	1850	16	1.12	2.42	0.90	0.91	0.16	15.91
6	2800	2500	12	1.29	1.66	0.90	0.91	0.16	15.91
7	3500	1200	16	1.56	0.32	1.12	-0.98	0.22	13.15
8	3500	1850	12	1.09	0.81	1.06	-0.50	0.24	12.39
9	3500	2500	14	1.31	1.39	1.03	-0.25	0.21	13.55

4. RESULTS AND DISCUSSION

The Taguchi method was successfully applied to conduct the nine different experiments. The results of the tests conducted on kerf width, surface roughness and HAZ are displayed in Tables 4, along with the relevant S/N ratios. When carrying out machining operations, it is usual practice to make achieving low kerf width, surface roughness and HAZ values to make ensuring a high level of quality and accuracy. So, for kerf width, surface roughness and HAZ, it's best if the data given is as low as possible.

The ratio of kerf width, should also be evaluated after the principal effects plots have been drawn (Fig 2). The monitoring features are organized with the use of an orthogonal matrix. The ratio of kerf width measurements, as represented in terms of the signal-to-noise ratio (S/N), are shown in Table 5.

Table 5. Response Chart for Ratio of kerf width Signal-to-Noise Ratios

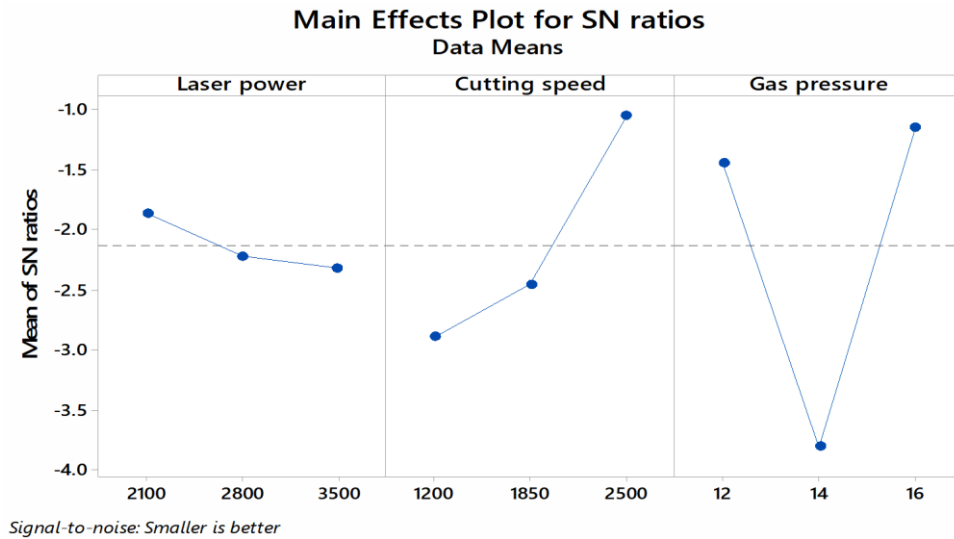| Level	LP (Watt)	CS (mm/min)	GP (bar)
1	1.310	1.407	1.183
2	1.300	1.373	1.570
3	1.320	1.150	1.177
Delta	0.020	0.257	0.393
Rank	3	2	1

Fig. 2. Plots of the main effects for Ratio of kerf width
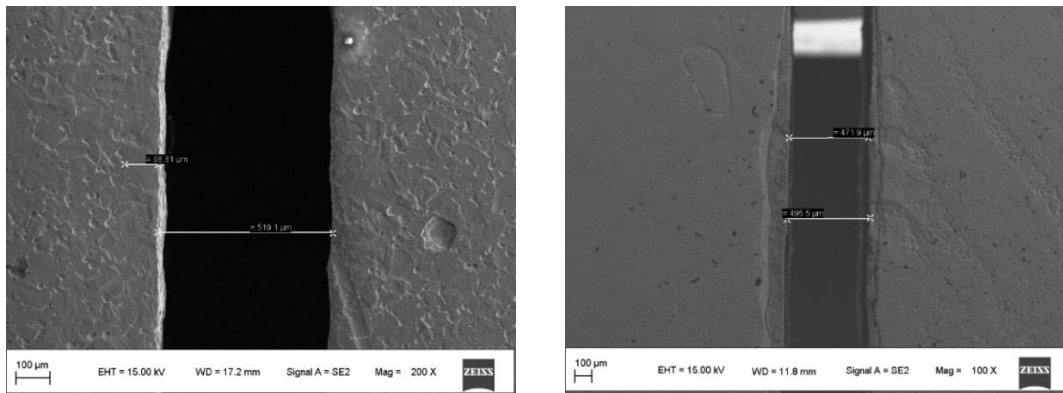

Fig. 3. Effect of laser process parameter on kerf width

In a similar manner, one should plot the primary impacts plots and evaluate the surface roughness. An orthogonal matrix is utilized to facilitate the organization of the monitoring characteristics. Table 6 presents the results of surface roughness measurements, which are also expressed in terms of the S/N ratio (Fig 4).

Table 6. Response chart for surface roughness signal-to-noise ratios

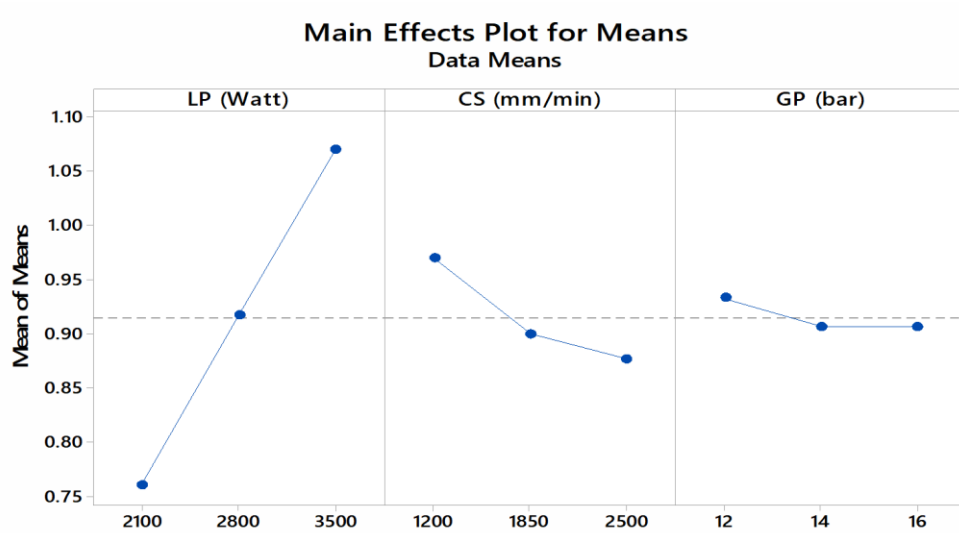| Level	LP (Watt)	CS (mm/min)	GP (bar)
1	0.7600	0.9700	0.9333
2	0.9167	0.9000	0.9067
3	1.0700	0.8767	0.9067
Delta	0.3100	0.0933	0.0267
Rank	1	2	3

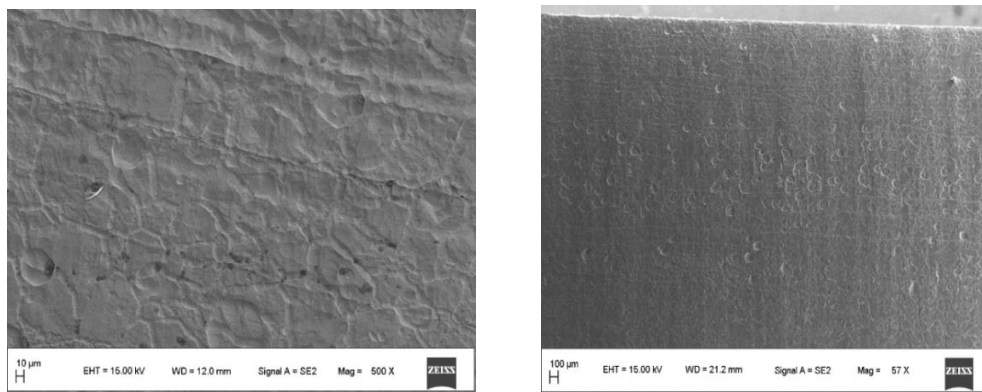Fig. 4. Plots of the main effects for Surface Roughness

Fig. 5. Effect of laser process parameter on surface roughness

After the principal effects plots have been drawn, the HAZ should also be assessed (Fig 6).
Control parameters are organized using an orthogonal matrix. Table 7 displays the HAZ
measurements as represented by the signal-to-noise ratio (S/N).

Table 7. Response chart for HAZ Signal-to-Noise ratios

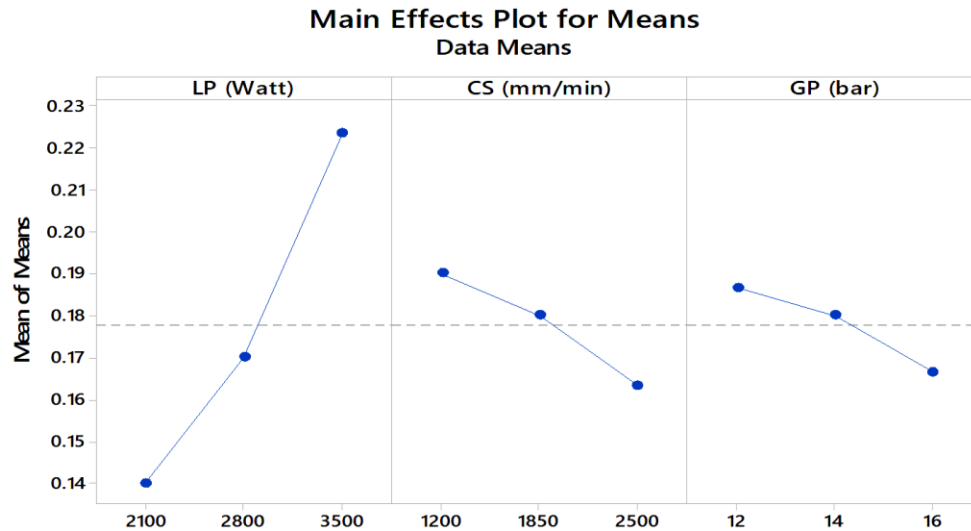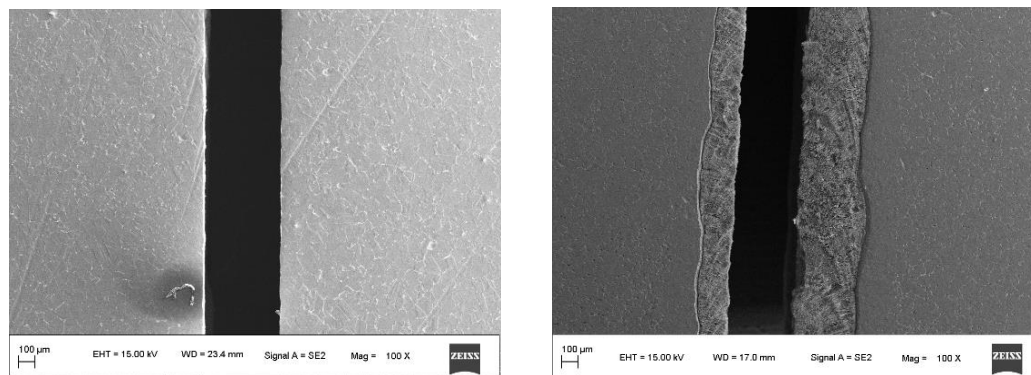| Level	LP (Watt)	CS (mm/min)	GP (bar)
1	17.14	14.50	14.74
2	15.42	15.13	15.02
3	13.03	15.96	15.83
Delta	4.10	1.47	1.08
Rank	1	2	3

Fig. 6. Plots of the main effects for HAZ

Fig. 7. Effect of laser process parameter on HAZ

During laser processing, the parameters that control the laser can have a substantial impact on the kerf width, surface roughness, and heat-affected zone (HAZ) of the material being processed. The kerf width, surface roughness, and HAZ are all crucial factors that can influence the quality and performance of materials that have been processed with a laser. The kerf width, surface roughness, and height at zone (HAZ) are all affected by the laser process parameters listed below.

Laser power: It was discovered that increasing the power intensity increase the kerf width. Greater melting and evaporation of material with higher laser power typically leads in deeper melting and greater HAZ. Because larger melt pools form and solidification rates increase, this can also lead to increased surface roughness. However, less intense lasers may cause uneven melting and lower surfaces roughness.

Cutting speed: It was discovered that reducing the cutting speed increase the kerf width. Rapid movement of the laser energy across the material at higher cutting speeds results in less heat generation and faster solidification, both of which contribute to a lower surface roughness. When cutting at extremely high speeds, there is a risk of partial melting and lower material removal rates, both of which may lead to an increased surface roughness.

Gas pressure: During laser cutting, the kerf width, surface roughness and HAZ can be changed by the type and flow rate of the gas. Having the right amount of gas flow can help to remove dirt and reducing the formation of oxides which can improve the quality of the surface. But too much gas flow can also cause turbulence and result in higher kerf width, surface roughness. So moderate value of gas pressure is suggested.

In order to achieve the desired kerf width, surface roughness, and HAZ characteristics, it is essential to optimize laser process parameters for a particular material and application, as the effects of these parameters can be complex and may vary depending on the specific material, laser system, and processing conditions.

5. VALIDATION OF EXPERIMENT

Predictions were made for the ratio of kerf width, Surface Roughness, and HAZ by utilizing the information obtained from the Taguchi method and applying it to the ideal circumstances. The Taguchi Method predicted that the kerf width would be 1.30, when the laser power was 2800 watts, the cutting speed was 2500 mm/min, and the gas pressure was 16 bar, while conducting the actual experiment, it was found that the ratio of kerf width is 1.12.

The Taguchi Method predicted a surface roughness of 1.08, where the laser power was 3500 watts, the cutting speed was 1850 mm/min, and the gas pressure was 12 bar. The surface roughness was measured 1.07 when the experiment was being performed. Similarly, the HAZ was predicted to be 0.083 using the Taguchi method, at 2100 watts of laser power, 2500 mm/min of cutting speed, and 16 bars of gas pressure, In the real experiment, under perfect conditions, measured a HAZ of 0.08.

Table 8. Confirmation Test for Ratio of kerf width, HAZ and Surface roughness

Output	LP	CS	GP	Predicted	Actual	%
Ratio of kerf	2800	2500	16	1.30	1.12	1.60
Surface roughness	3500	1850	12	1.08	1.07	1
HAZ	2100	2500	16	0.083	0.08	3.75

6. CONCLUSIONS

In this study, the parameter design of the Taguchi method was used to study and explain the relationship between kerf width, surface roughness, and HAZ in CO2 laser cutting operations. The main goal is to find the best combination of "laser power", "cutting speed", and "gas pressure" to get the best output qualities, such as "kerf width", "Ra", and "HAZ". The followingconclusions can be drawn from the experiments conducted for this study:

1. By varying the laser power, cutting speed, and gas pressure, the ideal processing conditions for reducing the ratio of kerf width were determined to be 2800 watts, 2500 mm/min, and 16 bars, respectively.

2. According to the research and findings, the laser power is the most crucial component in determining the appropriate ratio of kerf width.

3. Effective HAZ and Surface roughness characteristics were identified based on the analysis. The best HAZ and surface roughness can be achieved primarily by optimizing the laser's power.

4. The optimum conditions for reducing Surface roughness are 3500 watts of laser power, 1850 mm/min of cutting speed, and 12 bars of gas pressure. The optimal values for reducing HAZ are 2100 watts of laser power, 2500 mm/min of cutting speed, and 16 bar of gas pressure.

REFERENCES

[1] Senthilkumar, V., Adinarayanan, A., & Jagatheesan, K. (2023). Grey relational analysis (GRA) for optimization of CO2 laser cutting of Stainless Steel. Materials Today: Proceedings, 72, 2437-2442.

[2] Ma, G., Wu, D., Niu, F., & Zou, H. (2015). Microstructure Evolution and mechanical property of pulsed laser welded NI-based superalloy. Optics and Lasers in Engineering, 72, 39-46.

[3]   Hashim, M., Sarath Raghavendra Babu, K., Duraiselvam, M., & Natu, H. (2013). Improvement of wear resistance of Hastelloy C-276 through laser surface melting. Materials & Design (1980-2015), 46, 546-551.

[4] Madic, M., Petrovic, G., Petkovic, D., Antucheviciene, J., & Marinkovic, D. (2022). Application of a robust decision-making rule for comprehensive assessment of laser cutting conditions and performance. Machines, 10(2), 153.

[5] Hiwale, S., & Rajiv, B. (2021). *Experimental investigations of laser machining process parameters using response surface methodology.* Materials Today: Proceedings, 44, 3939-3945.

[6] Patidar, D., & Rana, R. (2018). *The effect of CO2 Laser Cutting parameter on mechanical & microstructural characteristics of high strength steel-A Review.* Materials Today: Proceedings, 5(9), 17753-17762.

[7] Dubey, A. K., & Yadava, V. (2008). *Laser Beam Machining—A Review.* International Journal of Machine Tools and Manufacture, 48(6), 609-628.

[8]   Santosh, S., Kevin Thomas, J., Pavithran, M., Nithyanandh, G., & Ashwath, J. (2022). *An experimental analysis on the influence of CO2 laser machining parameters on a copper-based shape memory alloy.* Optics & Laser Technology, 153, 108210.

[9]   Yongbin, Y., Bagherzadeh, S. A., Azimy, H., Akbari, M., & Karimipour, A. (2020). *Comparison of the artificial neural network model prediction and the experimental results for cutting region temperature and surface roughness in laser cutting of AL6061T6 alloy.* Infrared Physics & Technology, 108, 103364.

[10] Shrivastava, P. K., & Pandey, A. K. (2018). *Parametric optimization of multiple quality characteristics in laser cutting of Inconel-718 by using hybrid approach of multiple regression analysis and genetic algorithm.* Infrared Physics & Technology, 91, 220-232.

[11] Sharma, A., & Yadava, V. (2018). *Experimental Analysis of ND-YAG laser cutting of sheet materials – a review.* Optics & Laser Technology, 98, 264-280.

[12] Girdu, C. C., & Gheorghe, C. (2022). *Energy efficiency in CO2 laser processing of Hardox 400 material.* Materials, 15(13), 4505.

[13] Madic, M., Antucheviciene, J., Radovanovic, M., & Petković, D. (2017*). Determination of laser cutting process conditions using the preference selection index method.* Optics & Laser Technology, 89, 214-220.

[14] Gnanavelbabu, A., Arunachalam, V., Sunu Surendran, K. T., Rajkumar, K., & Anandhababu, E. (2020). *Optimization of CO2 laser cutting parameters for AA6061/B4C/HBN Hybrid Composites using Taguchi-based response surface methodology.* Lecture Notes in Mechanical Engineering, 111–122.

[15] Wang, J., Sun, Z., Gu, L., & Azimy, H. (2021). *Investigating the effect of laser cutting parameters on the cut quality of Inconel 625 using Response surface method (RSM).* Infrared Physics & Technology, 118, 103866.

[16] Hiwale, S., & Rajiv, B. (2021). *Experimental investigations of laser machining process parameters using response surface methodology.* Materials Today: Proceedings, 44, 3939–3945.

[17] Naresh, & Khatak, P. (2022). *Laser cutting technique: A literature review.* Materials Today: Proceedings, 56, 2484–2489.

[18] Santosh, S., Kevin Thomas, J., Pavithran, M., Nithyanandh, G., & Ashwath, J. (2022). *An experimental analysis on the influence of CO2 laser machining parameters on a copper-based shape memory alloy.* Optics & Laser Technology, 153, 108210.

[19] Zeilmann, R. P., & Conrado, R. D. (2022). *Effects of cutting power, speed and assist gas pressure parameters on the surface integrity cut by laser.* Procedia CIRP, 108, 367–371.

[20] Hasçalık, A., & Ay, M. (2013). *CO2 laser cut quality of Inconel 718 nickel – based superalloy.* Optics & Laser Technology, 48, 554–564.

[21] Hashim, M., Sarath Raghavendra Babu, K. E., Duraiselvam, M., & Natu, H. (2013). *Improvement of wear resistance of Hastelloy C-276 through laser surface melting.* Materials & Design (1980-2015), 46, 546–551.

[22] Shrivastava, P.K. and Pandey, A. K. (2018). *Parametric optimization of multiple quality characteristics in laser cutting of inconel-718 by using hybrid approach of multiple regression analysis and genetic algorithm.* Infrared Phy. Technol. 91, 220- 232.

[23] Madic, M., Antucheviciene, J., Radovanovic, M., & Petkovic, D. (2017). *Determination of laser cutting process conditions using the preference selection index method.* Optics & Laser Technology, 89, 214–220.

[24] Moradi, M., Mehrabi, O., Azdast, T., & Benyounis, K. Y. (2017). *Enhancement of low power CO2 laser cutting process for injection molded polycarbonate.* Optics & Laser Technology, 96, 208–218.

[25] Shrivastava, P.K. and Pandey, A. K. (2018). *Geometrical quality evaluation in laser cutting of inconel-718 sheet by using Taguchi based regression analysis and particle swarm optimization.* Infrared Phy. Technol. 89, 369-380.

[26] Anghel, C., Gupta, K. and Jen, T.C. (2019). *Analysis and optimization of surface quality of stainless-steel miniature gears manufactured by CO2 Laser cutting.* Optik. 203, 164049.

[27] Elsheikh, A.H., Deng, W. and Showaib, E.A. (2020) *Improving laser cutting quality of polymethylmethacrylate sheet: Experimental Investigation and Optimization,* Journal of Materials Research and Technology, 9(2), pp. 1325–1339.

[28] Sharifi, M. and Akbari, M. (2019). *Experimental investigation of the effect of process parameters on cutting region temperature and cutting-edge quality in laser cutting of AL6061T6 alloy.* Optik Int. J. Light Elec. 184, 457–463.

[29] Rosa, J. L., Robin, A., Silva, M. B., Baldan, C. A., & Peres, M. P. (2009). *Electrodeposition of copper on Titanium Wires: Taguchi Experimental Design Approach.* Journal of Materials Processing Technology, 209(3), 1181–1188.

[30] Rao, R. S., Kumar, C. G., Prakasham, R. S., & Hobbs, P. J. (2008). *The taguchi methodology as a statistical tool for biotechnological applications: A critical appraisal.* Biotechnology Journal, 3(4), 510–523.

[31] Rao, R. S., Prakasham, R. S., Prasad, K. K., Rajesham, S., Sarma, P. N., & Rao, L. V. (2004). *Xylitol production by candida sp.: Parameter optimization using Taguchi Approach.* Process Biochemistry, 39(8), 951–956.

[32] Prasad, B. (1997). *Book reviews: The transition to agile manufacturing—staying flexible for competitive advantage, edited by Joseph C. Montgomery and Lawrence O. Levine;* published by ASQC Quality Press, Milwaukee, Wisconsin ©1996 ISBN 0-87389-347-6. *Concurrent Engineering*, 5(3), 293–293.

[33] O'Connor, P. D. (1990). *Quality through design: Experimental design, off-line quality control and Taguchi's contributions, N. Logothetis and H. P. Wynn, Oxford University Press, 1990.* number of pages: 464, Quality and Reliability Engineering International, 6(2), 161–161.

[34] Nie, L. (2008). *Optimum experimental designs. A. C. Atkinson, A. N. Donev and R. D. Tobias, with SAS Oxford University Press*, Oxford, 2007. ISBN13: 978-0-19-929660-6, 978-0-19-929659-0. *Statistics in Medicine*, 27(28), 6034–6035.

[35] Fisher, H. L. (1956*). Rubber.* Scientific American, 195(5), 74–88.

[36] Woo, S. (2019). *Introduction to reliability design of mechanical/civil system.* Reliability Design of Mechanical Systems, 1–17.

BACK

International Journal of Engineering

Finite Element Modelling of Laboratory Tests on Reinforced Concrete Beams Containing Recycled Aggregate Concrete

A. J. Pawar*, M. Patel, S. R. Suryawanshi

Department of Civil Engineering, S. V. National Institute of Technology, Surat, India

A B S T R A C T

The predictive accuracy of the finite element (FE) based packages are broadly based on the compatibility of adopted non-linear numerical procedures and incorporated material models. However, the routine way to define concrete material is not applicable to the concretes containing substitute materials in place of conventional concrete ingredients. Therefore, in this work, appropriate definition of materials in terms of stress-strain relations have been utilized to simulate the experimental work of RC beams containing coarser fractions of recycled concrete aggregates (RCA). The entire work has been carried out into two phases; an experimental work and the simulation of experimental work using FEA package, ABAQUS. In the experimental part, three number of full-scaled beam specimens were tested to failure through four-point monotonous loading. The replacement level of natural coarse aggregates was taken as 0.0, 50 and 100% by direct substitution. In the simulation phase, in addition to laboratory evaluated properties like compressive stress, tensile stress and elastic modulus, the measured stress-strain relationship for reinforcing steel and constitutive relationship for recycled aggregate concrete (RAC) reported in the literature have been considered as an input. The stress-strain relationships of RAC selected from the literature has been treated as user defined model. Besides the strength, serviceability in terms of deflections, crack patterns and load deformation characteristics of simulated beams have been investigated and compared with those of laboratory tested beam specimens.

doi: 10.5829/ije.2023.36.05b.15

NOMENCLATURE

FEA	Finite element analysis	NA	Natural aggregate
RC	Reinforced concrete	NAC	Natural aggregate concrete
RCC	Reinforced cement concrete	LVDT	Linear variable differential transformer

1. INTRODUCTION

A good number of FEA packages have been developed to evaluate the response of RCC structural forms during last few decades. The performance in terms of accuracy of these packages are broadly based on the adopted non-linear numerical procedures and incorporated material models [1]. These models mainly categorised into two classes such as empirical models and continuum mechanics-based models [2]. Initially continuum mechanics-based models were confined to isotropic and homogeneous materials. However, with an advancement

in technology and broadened requirement, these theories have been extended to heterogeneous materials like concrete [3]. On the other hand, in the construction industry, sustainability become an urgent necessity of an hour, and to that end, utilization of waste products as a substitute material for concrete ingredients become evident [4]. Eventually, the use of recycled aggregates in concrete making and structural applications of such concrete is started gaining momentum [5, 6]. However, the analysis of such structural elements containing RAC requires special attention as the concrete models available in these softwares are not compatible with the modified properties and stress-strain relationships of RAC. Because RAC beams exhibit higher strains and deflection and lower or similar cracking moments than

*Corresponding Author Email: akshay4592@gmail.com (A. J. Pawar)

conventional ones [7, 8]. Nevertheless, some packages offer freedom to the users to use laboratory evaluated index properties and measured stress-strain relationships. ABAQUS is one of such softwares which offers freedom to users to use user-defined material-models with ease.

As discussed in the preceding paragraph, the use of FEA packages has become the essential component of the modern analysis and design procedures pertaining to civil engineering structures [9]. With the rapid growth of FE techniques and material constitutive models in the last decade, the numerical methods have become more significant, since they can successfully simulate difficult or even complicated cases [10]. An important part of numerical analysis has been the development of a numerical method that works well with measured uniaxial stress-strain relationships [11]. Computer programs like LS-Dyna, ABAQUS and ANSYS are being extensively used [12]. On the contrary, some analysis software's have the limitations regarding the simulation of appropriate support conditions. For instance, to establish the line contact in order to simulate the steel rollers as point loads and supports to carry out the analysis of four-point bending test of RCC beam specimens. The software is programmed in such a way that only finite dimensions can create the support and load contacts. Therefore, in some studies [13, 14] steel plates (finite dimensions) in place of steel rollers were considered to define and simulate the support condition (as no alternative left to simulate rollers) even though the companion laboratory tests on RCC beams consist of steel rollers. Besides this, the input parameters assigned prior to simulation of structural components or structure as a whole plays very crucial role especially when alternate materials for concrete ingredients are to be used aiming sustainable development [15, 16]. It should be noted that the routine way to define concrete material is not applicable to the concretes containing substitute materials in place of conventional ingredients. In such a scenario, it becomes inevitable to carry out the simulation in the way the user manual administers. Few software offer liberty to the users to describe material behaviours employing measured stress-strain relationships as an input.

Typically, a FEA package is deemed to be competent in producing reasonable predictions when the variation between the anticipated and the experimentally measured values of certain structural attributes is less than 20% of the measured values, such structural characteristics typically include the load vs. displacement profiles, the load-carrying capacity, etc. and the qualitative behaviour pattern matches, such as the crack patterns at various load stages are also considered. Furthermore, FEA software is called objective and generic when it can accurately estimate structural behaviour for any structural concrete setup

without recalibrating the constitutive model or parameters [3].

In this work, ABAQUS was employed to simulate numerically the experimental work of RC beams of concrete containing coarse RCA, subjected to pure flexure failure. To ascertain the efficacy of the FE model, the typical constitutive model for RCA-concrete available in literature was examined with the corresponding experimental results of the beam specimens. Moreover, the flexural behaviour of beams obtained from the numerical-analysis was compared with the measured results in terms of the flexure strength, load deflection behaviour and crack patterns.

2. EXPERIMENTAL INVESTIGATION

In this experimental investigation, total three number of beam specimens were cast and tested to the failure in order to assess the structural behaviour of RCA-concrete beams. All the beam specimens were 2100 mm long and designed for a cross-section of 125 mm width and 250 mm depth according to Indian Standards IS 456 [17], and were tested over 1800 mm simply supported span with 150 mm overhangs on each side. For all the beams, the shear-span of 600 mm was considered. The four-point loading was applied to the beam specimens in order to get no shear force in the region of constant moment. The region of constant moment was defined 600 mm, which was equal to the one-third of effective span. The nominal top reinforcement was curtailed in the region of constant moment to eliminate the effect of it on pure flexure failure, as the beam section was desired to be singly reinforced. Thermo-Mechanically Treated (TMT) steel rebars conforming to IS 1786 [18] were used to form cages. The measured yield strength of Fe500 grade rebar was 500 MPa. The reinforcement details of the beam specimens are depicted in Figure 1.

The concrete containing RCA extracted from the debris of demolished RCC structures was used to cast test specimens. The control concrete mixture containing natural coarse aggregates was designed by absolute volume method, conforming IS 10262 [19] whereas the mix for RAC was designed by the direct weight replacement method (DWRM). In the DWRM, the natural coarse aggregates were replaced with an equivalent weight of recycled coarse aggregate particles. The weight proportion of recycled coarse aggregates in
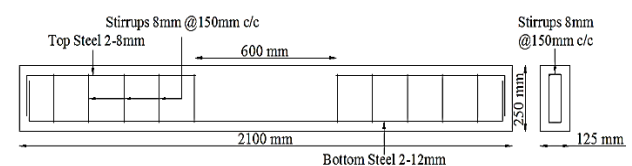

Figure 1. Typical reinforcement detail

TABLE 1. Mixture composition (in terms of ratios by weight) and measured properties of the NAC and the RCA-concretes

Mix Id	RCA replacement level	Cement	Mixing Water	Fine aggregates	Coarse NA (4.75-20 mm)	Coarse RCA (4.75-20 mm)	HRWRA (% by weight of cement)	Compressive strength (MPa)
R0	0	1.0	0.45	1.92	2.82	0.00	1.0	30.00
R50	50	1.0	0.45	1.92	1.41	1.41	1.0	28.50
R100	100	1.0	0.45	1.92	0.00	2.82	1.0	26.50

TABLE 2. Simmary of test and simulation results

| Beam Id	Replacement ratio (%)	Measured ultimate load (kN)	Ultimate load predicted by ABAQUS (kN)	Measured displacement at ultimate load (mm)	Displacement at ultimate load predicted by ABAQUS (mm)
R0	0	84.00	87.72	14.10	14.41
R50	50	80.50	84.37	12.96	13.70
R100	100	78.00	81.65	12.01	12.40

the total coarse aggregates of the concrete mix is specified as the recycled coarse aggregate replacement percentage. The replacement level of natural coarse aggregates with RCA in percentage was as follows: 0.0, 50 and 100%. Control concretes are identified in this investigation by the generic name of NAC whereas the concretes containing full fractions of the recycled coarse aggregates are identified by the generic name of RCA-concrete. Except for substitution of the natural coarse aggregate particles with the recycled coarse aggregate, the other constituents in these two concrete types were nominally the same. The mixture composition and concrete compressive strength using 150 x 300 mm cylindrical specimens of the NAC and the RCA-concrete used in the experimental programme are given in Table 1.

The first placeholder in the nomenclature of the beam represents replacement of natural coarse aggregate in concrete. The second placeholder (digits) indicates the level of replacement in percentage. For example, in the beam specimen R100 indicate 100% replacement of natural coarse aggregate.

Figure 2. Schematic test set-up for beam tests

After 24 hours of casting, the formwork was removed, and all the beam specimens were kept in a normal environment condition, enclosed with wet jute gunny bags until they were tested at 28 days of age. The beam specimens were surface dried after 28 days of curing, followed by application of a single layer of white wash to facilitate detection of crack formation and growth. The test setup for a typical beam in four-point loading across a simply supported span of 1800 mm is illustrated in Figure 2. On the side faces of the beams, an orthogonal grid of lines spaced 50 mm vertically and 100 mm horizontally was marked to aid with crack tracing. Each specimen was tested in a load frame of capacity 2000 kN in order to evaluate load carrying capacity of the beam specimens. The monotonically increased load was applied on the top face of the beams with the help of a 1000 kN capacity hydraulic jack until the beam failed. Before the actual loading, preloading was performed to ensure that the load cell and LVDT sensor function normally. The applied load was measured with the load cell. At the load point, two rollers were used to transfer equal applied load to each support through the steel beam arrangement as seen in Figure 2. Hinge and roller supports are illustrated in Figure 2 and the deflections at the load-point were measured using LVDT.

3. THE FINITE ELEMENT MODELLING

A FEA package is known for realistic predictions of the behaviour of structural forms in terms of structural characteristics. Load carrying capacity, load-deformation, moment-curvature relations and pattern matches like the crack patterns corresponding to different load stages and failure modes are some of them. Moreover, it should be capable of predicting the realistic behaviour of any structural form without recalibration. The main requirements of FEA modelling are as follows: 1) to adopt a constitutive relationship to
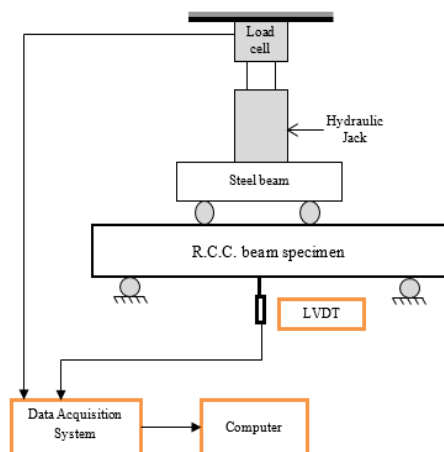
describe the material nonlinearity of concrete, steel rebars and their mutual interactions; 2) to incorporate a nonlinear numerical procedure that is effectively capable of implementing internal stresses redistribution forced by material nonlinearity against imposed external loadings plus a numerical description on cracking process.

Though the peak stress value is assumed to be implicit due to the gradual degradation of the stiffness related to residual material strength after a peak stress yet the numerical procedural scheme adopted by most of the softwares were developed independent of material models. The majority of FEA packages employed an iterative procedures based on numerical techniques like Newton-Raphson method. The iterative procedure is to account for the checks for redistribution of stresses during crack openings and crack closure, besides the simultaneous checks on convergence in each iteration. The iterations are repeated till the convergence criterion met resulting into attainment of predefined minimum value of residual forces estimated from the use of equilibrium equations.

3. 1. Geometry Definition There are several approaches available to create geometry of an element in ABAQUS out of which the simple objects method has been used. The 3D geometry of the element is created in create part tab by taking modelling space and element type. The cross section (125 mm thick and 250 mm deep) of the concrete beam was created and the beam was extruded in the direction of length. By adopting the prescribed procedure to create elements, geometrical model of beam specimens created in ABAQUS is depicted in Figure 3 (a). For the simplicity of assembling the elements, datum planes were created using create partition cell tool.

The steel reinforcement (both main steel and stirrups) was modelled as wire elements in ABAQUS as per the experimental reinforcement detailing. Elements of reinforcement i.e., tension bar, top bar and stirrups were created individually under the create part section and assigned a cross section area of these wire elements as a truss element. These elements were assembled and rearranged using translate, rotate and linear pattern instance tool in the assembly section by providing required spacing, effective covers and other details according to reinforcement assembly. The 8 mm diameter bar was used as web reinforcement and top bars in the beams whereas the 12 mm diameter bar was used as a main steel provided at the bottom. The nominal top reinforcement in the compression zone was curtailed in order to achieve the effect of singly reinforced section in predefined region of pure bending as described earlier. The reinforcement cage similar to actually used in the beam is modelled which is shown in Figure 3(b).
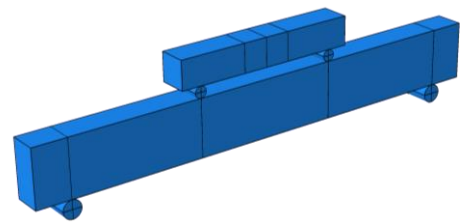
(a) Geometrical modelling of beams and supports
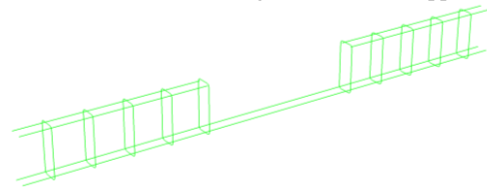
(b) Configuration of reinforcement

Figure 3. Geometry of the beam specimen created in ABAQUS

3. 2. Material Definition In the FE analysis part, the brittle-cracking model available in ABAQUS is employed as a material model. This yields better results when the behaviour of concrete material is governed by tensile cracking. The behaviour in compression is also idealised to be linear before cracking. In order to detect the crack initiation and propagation, a simple Rankine yield criterion has been utilised. According to Rankine yield criterion, the material starts cracking when resultant principal stress crosses the concrete tensile-strength. It is obvious that the crack surface is perpendicular to the major principal tensile stress. Subsequently other developed cracks are normal to the existing crack at the same location. Unlike other models, in this model, crack closing and reopening is allowed. Crack gets bridged as soon as the resultant principal stress becomes compressive after redistribution of stress. Moreover, it uses smeared crack model philosophy to characterize the non-ductile response of concrete.

The Brittle-cracking model includes two modes of failures as follows: 1) Mode-I based on tension-stiffening and Mode-II is on the basis of shear-retention. In strain-softening the stress linearly goes on decreasing to zero. As per the model, in the post-peak region, the strain is 10 times that of failure strain when the stress resumes to zero value. The crack initiation is controlled by Mode-I while the post-peak cracks are governed by both the modes. To model shear-behaviour, the post-cracking shear-modulus is defined in terms of the fractions of non-cracked shear-modulus. The model treats shear-retention in terms post-cracking shear-stiffness which is defined in terms of opening strain normal to crack.

3. 2. 1. Concrete ABAQUS offers freedom to user to define the material of practical relevance. It defines the concrete behaviour in terms of Concrete

Damage Plasticity (CDP) model. The other input parameters should be evaluated in the laboratory or idealised values reported in the literature may be used in absence of data. However, the real values are expected to use as an input in order to get accurate analysis.

The stress-strain relation of concrete used in the numerical-analysis should to be determined by testing the specimen in the laboratory. Figure 4 depicts the window to enter user defined material definition in the form of compression test stress-strain data and damage parameter on the basis of inelastic strain. Likewise, tensile test stress-strain data and damage parameter of the material model can be fed up to define the CDP model for concrete.

In this investigation, typical constitutive model for RAC was proposed by Suryawanshi et al. [11] which is used to define the concrete behaviour as follows:

$$\bar{\sigma} = a(\bar{\varepsilon}) + b(\bar{\varepsilon})^2 + c(\bar{\varepsilon})^3 + d(\bar{\varepsilon})^4 \tag{1}$$

where, $\bar{\sigma}$ is the normalized stress, $\bar{\varepsilon}$ is the normalized strain. Constants a, b, c and d were determined by regression analysis of test data. Constant a has definite meaning and may be defined in terms of percentage replacement of NA. Other coefficients b, c and d were expressed in relation of a.

3. 2. 2. Steel Reinforcement   As discussed in the preceding sections, ABAQUS allow users to enter the stress-strain relationship of steel as input data so that the software can effectively simulate the behaviour of reinforcement steel. Figure 5 shows the appearance of dialogue box after entering the measured stress-strain values. It should be noted that, the ABAQUS accepts only inelastic strain values and corresponding stress
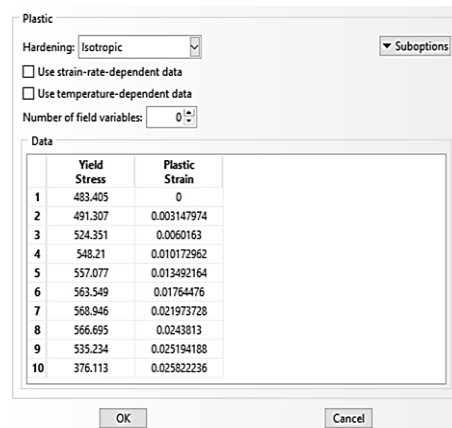

Figure 4. Details of stress-strain relations for concrete as an input parameter

Figure 5. Details of measured stress-strain relations for reinforcement as an input parameter

values. The value of inelastic strain is determined as a difference of total strain and elastic strain.

3. 3. Modeling of Support and Load Points Unlike few FEA packages, ABAQUS allows to model and simulate curved elements like steel rollers used at loading points and supporting points through perfect contact as illustrated in Figure 6. The force was applied to beam by displacement controlled strategy as per prescribed deformation rate at the centre-point of the top surface of the spreader beam. The supports, in the form of two steel rollers used in experiments were modelled by appropriate boundary conditions on a line of contact. The supports were assumed as a rigid body and restricted to a predefined point as a reference. The movement reference point in vertical direction was restrained. Similarly, the steel rollers were modelled beneath the spreader beam used to apply load on the RC beam. The monitoring point to record the magnitude of applied load was placed at the centre-point of top surface of spreader beam. The position of the deflection monitors was the point where the LVDT was mounted in the prototype test.

For the structured meshes, the ABAQUS solver allows the usage of first-order hexahedral components; however, for unstructured meshes it permits the use of both first and second-order tetrahedral elements. 8-noded 3D hexahedral elements in the form of bricks (C3D8I) were employed in this investigation. The behaviour of traditional 8-noded elements is prohibited from being over rigid in bending by internally incompatible deformation modes, besides the normal degrees of freedom for displacement. The mesh being utilised for the concrete has an impact on how these components are implemented in the FE model. This work made use of the 3D linear truss (T3D2) element type with a mesh size of 10 mm. The geometry of a simulated beam with produced mesh elements is shown in Figure 6.
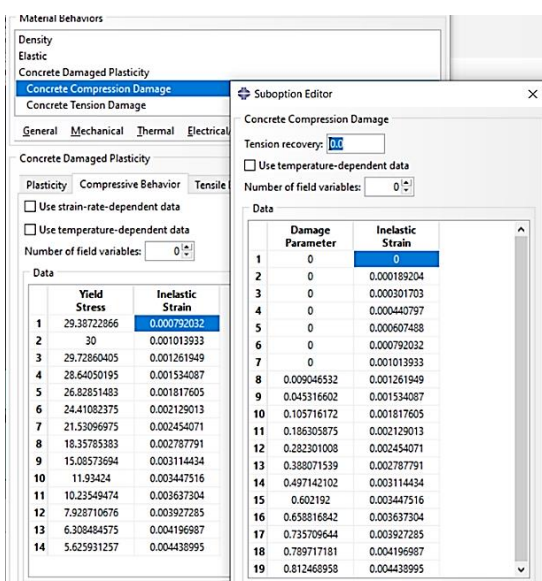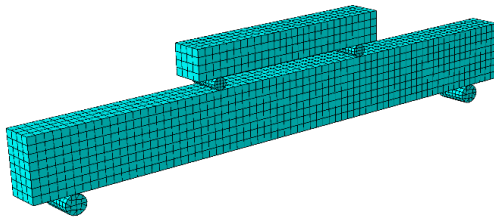
Figure 6. Finite element mesh of assembly

## 4. RESULT AND DISCUSSION

4. 1. Load Deflection Behavior   The results of beam tests are compiled in Table 2 for reference and compared against results obtained from the ABAQUS analysis. It is clearly seen that the load carrying capacity of the beam when analysed by ABAQUS software is found in the close range to that of experimentally obtained results. It has been observed that the load carrying capacity of the RAC-beam is marginally lesser and slightly higher deflections than that of the NAC-beam. The ABAQUS analysis also indicate similar trend of reduction in load carrying capacity and increased deflections on higher replacement levels. Recent literature review on experimental flexure tests performed by Seara-Paz et al. [20] and Pradhan et al. [8] also agree that load carrying capacity of RAC-beam is lesser and shows higher deflection compared to NAC-beam. This may be attributed to the reduction of modulus of elasticity of concrete corresponding to a higher degree of replacement of NA [21].

The comparison of experimentally obtained load-deflection curves for beam specimens R00, R50 and R100 respectively are shown in Figure 7(a). A side-by-side comparison of ABAQUS analysis load-deflection curves for each beam is also presented in Figure 7(b). The trends of load-deformation characteristics in both the analysis are similar. The RAC beams had a lesser cracking load than the NAC beams due to the presence of two types of interfacial transition zones (ITZ) [22]. The ITZ between residual mortar and virgin aggregate in and the ITZ between new mortar and residual mortar. On the contrary, the NAC has one ITZ (between fresh mortar and virgin aggregate). Moreover, the RAC beams exhibited lower stiffness after the cracking load, which may be attributed to the RCA-concrete having comparatively lower modulus of elasticity to that of the NAC [23].

Figure 8(a), (b) and (c) reveals load-deflection relationships of tested beam specimens correspond to different RCA replacement levels, 0.0, 50 and 100%. The load-deflection relationships generated by ABAQUS software are also shown in Figure 8(a), (b) and (c). After cracking, each specimen behaved almost linearly until the tension bar began to yield. Each specimen thereafter
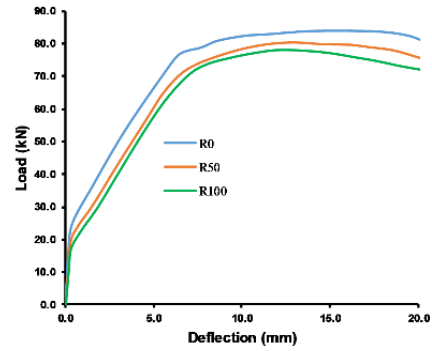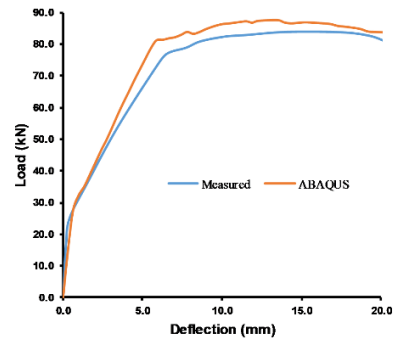

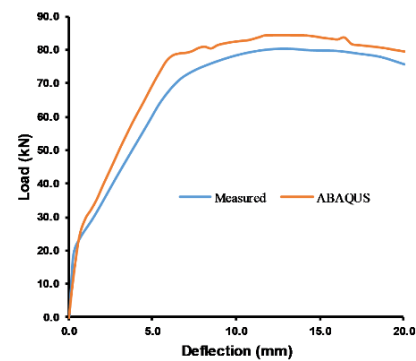(a) Measured load-deflection relationship
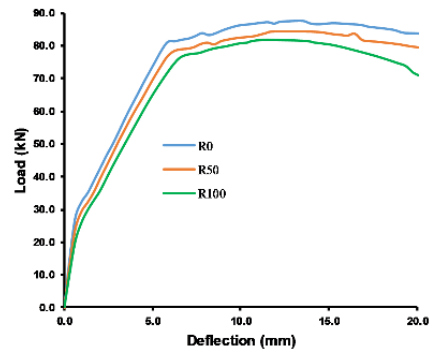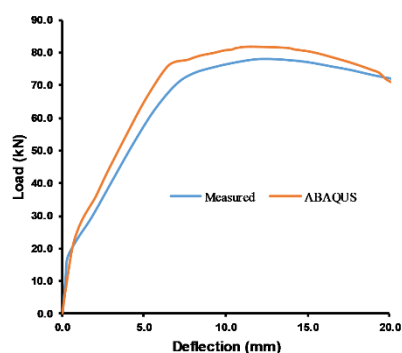

(b) Predicted load-deflection relationship

Figure 7. Comprehensive comparison of trends of measured and predicted load-deflection relationships


(a) Beam R00

(b) Beam R50

(c) Beam R100

Figure 8. Comparison of measured and predicted load-deflection relationships of various beams

R0

R50

R100

Figure 9. Comparison of observed creack patterns with ABAQUS simulated principal tensile strain profiles

exhibited nonlinear behavior until it reached its failure load. The beams then reached a ductile plateau which is typical behaviour of RCC flexural member. After enough rotation of the developed plastic-hinge, extreme stresses are developed in the compression zone of the specimens, culminating in crushing failure.

4. 2. Cracking Behavior of RCA-Concrete Beam

The cracking behavior of the beams in terms of the number, the orientation, and the extent of the cracks, was monitored throughout the loading history. The first crack started forming from the soffit of beam in the mid-span region, the region of maximum bending moment. The first crack occurred at 25 kN in R00-beam whereas the FEA simulation revealed it at 27.32 kN. Similarly, the first crack formed at 17.21 kN in R100-beam and at 25.78 kN in simulated beam. All beam specimens containing RCA-concrete showed the tendency of first crack formation comparatively at lower load to that of beam containing NAC. With increase in applied load, additional flexural cracks were formed between the loading point and the support points. All these cracks propagated towards the compression zone revealed the typical crack-pattern of inclined flexure-shear cracks. It is clearly seen that the R00-beams has the least number but prominent cracks (Figure 9), whereas the R100-beam comparatively has a greater number of minor cracks. The findings of this investigation were in good agreement with observations of past study [8], in which the cracks in the RCA beams were closely spaced than in the NA beams. This might be due to the weakened interfacial transition zone of RCA between the new mortar and the old attached mortar. Besides the experientially observed cracking patterns, the bands of principal tensile strains revealed in ABAQUS analysis also presented in Figure 9.

On the contrary, it generates the bands of principal tensile strains [24]. The formation of tensile strain bands with specific colour to represent certain magnitude of
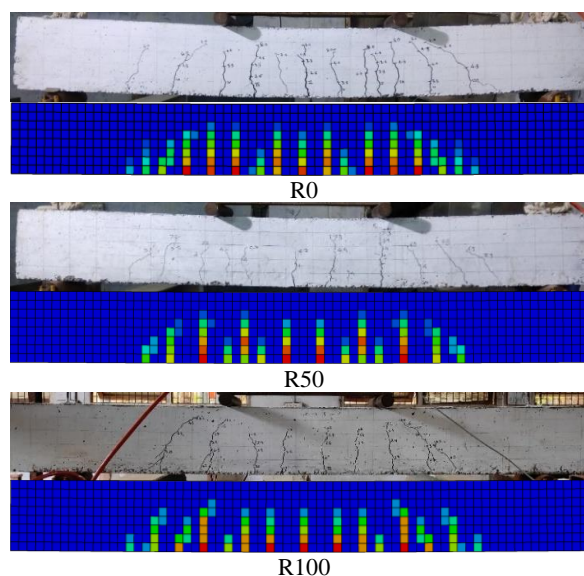
strains can be compared with the actual crack patterns observed during experiments. The comparison of crack patterns of beams with different replacement levels of RCA is shown in Figure 9. along with the principal tensile strain patterns generated by ABAQUS. The trend of the principal tensile strain patterns generated by ABAQUS is comparable with the experimentally observed crack patterns.

5. CONCLUSIONS

In this comparative study, the flexural member was numerically investigated and compared with the results of experimental study. Based on the experimental findings and results of numerical analysis, the following conclusions have been drawn.

1. The comparison of ABAQUS results and experimental observations revealed no major differences in the load carrying capacities of the beams. The trend of reduction in load carrying capacity and increasing mid-point deflections with increased replacement level in both the investigations are similar.

2. The load deformation characteristics revealed by ABAQUS simulation is significantly in match with that of experimentally measured load-deformation relationships. Thus indicating the importance of well define material definitions in terms of measured stress-strain relations on yield of numerical simulations.

3. Unlike other FEA packages, ABAQUS does not generate crack patterns. However, the crack patterns observed during experiments can be correlated with

the principal tensile strain profiles generated through numerical simulation. The cracking patterns and principal tensile strain profiles are found comparable.

4. Besides, correct material definitions, other input parameters in terms of index properties of materials has a control on the quality of simulation.

5. Geometric definition, well defined support conditions and appropriate selections of finite elements are the major factor influencing the outcomes of FEA analysis.

6. REFERENCES

1. Buyukozturk, O. and Shareef, S.S., "Constitutive modeling of concrete in finite element analysis", *Computers & structures*, Vol. 21, No. 3, (1985), 581-610. https://doi.org/https://doi.org/10.1016/0045-7949(85)90135-X

2. Pawar, A.J. and Suryawanshi, S., "Comprehensive analysis of stress-strain relationships for recycled aggregate concrete", *International Journal of Engineering, Transactions B: Applications*, Vol. 35, No. 11, (2022), 2102-2110. https://doi.org/10.5829/ije.2022.35.11b.05

3. Cotsovos, D.M., Zeris, C.A. and Abbas, A.A., "Finite element modeling of structural concrete", in Proceedings of the 2nd International Conference on Computational Methods in Structural Dynamics & Earthquake Engineering., (2009).

4. Yasin Mousavi, S., Tavakkoli, A., Jahanshahi, M. and Dankoub, A., "Performance of high-strength concrete made with recycled ceramic aggregates (research note)", *International Journal of Engineering, Transactions C: Aspects*, Vol. 33, No. 6, (2020), 1085-1093. https://doi.org/10.5829/ije.2020.33.06c.05

5. Silva, R., De Brito, J. and Dhir, R., "Use of recycled aggregates arising from construction and demolition waste in new construction applications", *Journal of Cleaner Production*, Vol. 236, (2019), 117629. https://doi.org/https://doi.org/10.1016/j.jclepro.2019.117629

6. Masne, N. and Suryawanshi, S., "Effect of replacement ratio on torsional behaviour of recycled aggregate concrete beams", *International Journal of Engineering, Transactions A: Basics*, Vol. 36, No. 4, (2023), 659-668. doi: 10.5829/ije.2023.36.04a.07.

7. Kang, T.H.-K., Kim, W., Kwak, Y.-K. and Hong, S.-G., "Flexural testing of reinforced concrete beams with recycled concrete aggregates", *ACI Structural Journal*, Vol. 111, No. 3, (2014). https://doi.org/10.14359/51686622

8. Pradhan, S., Kumar, S. and Barai, S.V., "Performance of reinforced recycled aggregate concrete beams in flexure: Experimental and critical comparative analysis", *Materials and Structures*, Vol. 51, (2018), 1-17. https://doi.org/10.1617/s11527-018-1185-0

9. Cotsovos, D.M. and Kotsovos, M.D., "Constitutive modelling of concrete behaviour: Need for reappraisal", *Computational Methods in Earthquake Engineering*, Vol. 21, (2011), 147-175. https://doi.org/10.1007/978-94-007-0053-6_7

10. Raveendra, B.R., Benipal, G.S. and Singh, A.K., "Constitutive modelling of concrete: An overview", (2005).

11. Suryawanshi, S., Singh, B. and Bhargava, P., "Equation for stress–strain relationship of recycled aggregate concrete in axial compression", *Magazine of Concrete Research*, Vol. 70, No. 4, (2018), 163-171. https://doi.org/10.1680/jmacr.16.00108

12. Masne, N. and Suryawanshi, S., "Analytical and experimental investigation of recycled aggregate concrete beams subjected to pure torsion", *International Journal of Engineering, Transactions A: Basics*, Vol. 35, No. 10, (2022), 1959-1966. https://doi.org/10.5829/ije.2022.35.10a.14

13. Yuan, S., Liu, Z., Tong, T. and Fu, C.C., "A pilot study on structural responses of normal concrete-uhpc composite bridge decks w/wo rebars through an experimental-numerical approach", *Advances in Civil Engineering*, Vol. 2020, (2020), 1-21. https://doi.org/10.1155/2020/8816337

14. Tambusay, A. and Suprobo, P., "Predicting the flexural response of a reinforced concrete beam using the fracture-plastic model", *Journal of Civil Engineering*, Vol. 34, No. 2, (2019), 61-67. https://doi.org/10.12962/j20861206.v34i2.6470

15. Bouzaiene, A. and Massicotte, B., "Hypoelastic tridimensional model for nonproportional loading of plain concrete", *Journal of Engineering Mechanics*, Vol. 123, No. 11, (1997), 1111-1120. https://doi.org/10.1061/(ASCE)0733-9399(1997)123:11(1111)

16. Chen, W., "Plasticity in reinforced concrete, mcgraw-hill", New York, NY, USA, (1982).

17. IS456, I.S.C., "Plain and reinforced concrete—code of practice (fourth revision)", *Bureau of Indian Standards, Manak Bhavan*, Vol. 9, (2000).

18. BIS, I., "Indian standard for high strength deformed steel bars and wires for concrete reinforcement", *Bureau of Indian Standards, New Delhi*, (2008).

19. 10262:, I., *Concrete mix proportioning–guidelines (second revision)*. 2019, IS: 10262, Bureau of Indian Standards New Delhi, India.

20. Seara-Paz, S., González-Fonteboa, B., Martínez-Abella, F. and Eiras-López, J., "Flexural performance of reinforced concrete beams made with recycled concrete coarse aggregate", *Engineering Structures*, Vol. 156, (2018), 32-45. https://doi.org/10.1016/j.engstruct.2017.11.015

21. Chen, X., Zhang, Z., Xu, Z., Wu, Q., Fan, J. and Zhao, X., "Experimental analysis of recycled aggregate concrete beams and correction formulas for the crack resistance calculation", *Advances in Materials Science and Engineering*, Vol. 2022, (2022). https://doi.org/10.1155/2022/1466501

22. Deng, Z., Sheng, J. and Wang, Y., "Strength and constitutive model of recycled concrete under biaxial compression", *KSCE Journal of Civil Engineering*, Vol. 23, (2019), 699-710. https://doi.org/10.1007/s12205-018-0575-8

23. Arezoumandi, M., Smith, A., Volz, J.S. and Khayat, K.H., "An experimental study on flexural strength of reinforced concrete beams with 100% recycled concrete aggregate", *Engineering Structures*, Vol. 88, (2015), 154-162. https://doi.org/10.1016/j.engstruct.2015.01.043

24. Earij, A., Alfano, G., Cashell, K. and Zhou, X., "Nonlinear three–dimensional finite–element modelling of reinforced–concrete beams: Computational challenges and experimental validation", *Engineering Failure Analysis*, Vol. 82, (2017), 92-115. https://doi.org/https://doi.org/10.1016/j.engfailanal.2017.08.025

Persian Abstract

چکیده

دقت پیش‌بینی بسته‌های مبتنی بر المان محدود (FE) به طور گسترده بر اساس سازگاری رویه‌های عددی غیرخطی اتخاذ شده و مدل‌های مواد گنجانده شده است. با این حال، روش معمول برای تعریف مواد بتن برای بتن های حاوی مواد جایگزین به جای مواد بتن معمولی قابل اجرا نیست. بنابراین، در این کار، از تعریف مناسب مواد از نظر روابط تنش-کرنش برای شبیه‌سازی کار تجربی تیرهای RC حاوی بخش‌های درشت‌تر از سنگدانه‌های بتن بازیافتی (RCA) استفاده شده است. کل کار در دو مرحله انجام شده است. یک کار آزمایشی و شبیه سازی کار آزمایشی با استفاده از بسته ABAQUS. ،FEA در بخش آزمایشی، سه نمونه تیر با مقیاس کامل از طریق بارگذاری یکنواخت چهار نقطه‌ای برای شکست مورد آزمایش قرار گرفتند. سطح جایگزینی سنگدانه های درشت طبیعی با جایگزینی مستقیم ۰.۰، ۵۰ و ۱۰۰ درصد در نظر گرفته شد. در مرحله شبیه سازی، علاوه بر خواص آزمایشگاهی ارزیابی شده مانند تنش فشاری، تنش کششی و مدول الاستیک، رابطه تنش-کرنش اندازه گیری شده برای فولاد تقویت کننده و رابطه سازنده برای بتن سنگدانه های بازیافتی (RAC) گزارش شده در ادبیات به عنوان ورودی در نظر گرفته شده است. . روابط تنش-کرنش RAC انتخاب شده از ادبیات به عنوان مدل تعریف شده توسط کاربر در نظر گرفته شده است. علاوه بر استحکام، قابلیت سرویس از نظر انحراف، الگوهای ترک و ویژگی‌های تغییر شکل بار تیرهای شبیه‌سازی شده بررسی شده و با نمونه‌های تیر آزمایش‌شده آزمایشگاهی مقایسه شده است.

BACK

Article

Constrained Static/Dynamic Economic Emission Load Dispatch Using Elephant Herd Optimization

Rajagopal Peesapati [1], Yogesh Kumar Nayak [2], Swati K. Warungase [3] and Surender Reddy Salkuti [4],*

[1] Department of Electrical and Electronics Engineering, Raghu Engineering College, Visakhapatnam 531162, India; rajgopal.peesapati@raghuenggcollege.in

[2] Department of Electrical Engineering, Government Engineering College, Keonjhar 758002, India; yogeshnayak_fee@gcekjr.ac.in

[3] Department of Electrical Engineering, K K Wagh Institute of Engineering Education and Research, Nashik 422011, India; swarungasethete@gmail.com

[4] Department of Railroad and Electrical Engineering, Woosong University, Daejeon 34606, Republic of Korea

* Correspondence: surender@wsu.ac.kr

Abstract: The rapid growth in greenhouse gases (GHGs), the lack of electricity production, and an ever-increasing demand for electrical energy requires an optimal reduction in coal-fired thermal generating units (CFTGU) with the aim of minimizing fuel costs and emissions. Previous approaches have been unable to deal with such problems due to the non-convexity of realistic scenarios and confined optimum convergence. Instead, meta-heuristic techniques have gained more attention in order to deal with such constrained static/dynamic economic emission load dispatch (ELD/DEELD) problems, due to their flexibility and derivative-free structures. Hence, in this work, the elephant herd optimization (EHO) technique is proposed in order to solve constrained non-convex static and dynamic ELD problems in the power system. The proposed EHO algorithm is a nature-inspired technique that utilizes a new separation method and elitism strategy in order to retain the diversity of the population and to ensure that the fittest individuals are retained in the next generation. The current approach can be implemented to minimize both the fuel and emission cost functions of the CFTGUs subject to power balance constraints, active power generation limits, and ramp rate limits in the system. Three test systems involving 6, 10, and 40 units were utilized to demonstrate the effectiveness and practical feasibility of the proposed algorithm. Numerical results indicate that the proposed EHO algorithm exhibits better performance in most of the test cases as compared to recent existing algorithms when applied to the static and dynamic ELD issue, demonstrating its superiority and practicability.

Keywords: energy management; economic load dispatch; artificial intelligence; elephant herd optimization

1. Introduction

1.1. Overview

One of the key issues with the power dispatch system is the ELD, which aims to schedule the active power of the CFTGU as efficiently as possible while adhering to certain equality and inequality constraints. The efficient allocation of generators leads to minimizing electricity costs for the end consumer, which is achieved via the effective solution methodology [1]. Various approaches have frequently been applied to the ELD problem in the past, such as genetic algorithms (GA), sequential quadratic programming (SQP) and evolutionary programming (EP) [2,3]. These approaches are fast and require derivatives of their fitness function, but cannot successfully solve large and complex problems such as ELD with VPE and ramp rate limits, as the Hessian or Gradient matrix is too difficult to form [4,5]. Additionally, EPs involve long computational times while handling composite constraints. In view of this, quantum bits can be incorporated into EP

to overcome composite constraints and to avoid local minima in the solution [6]. Likewise, in the recent past, algorithms such as an improved genetic algorithm with multiplier updating (IGAMU) [7], self-tuning hybrid differential algorithm (HDE) [8], anti-predatory particle swarm optimization (AP-PSO) [9], and EP with mutations (MEP) [10] have gained importance in solving the ELD problem. Further, algorithms such as PSO [11], evolutionary strategy optimization (ESO) [12] artificial bee colony (ABC) algorithm [13], hybrid quantum mechanics-inspired PSO (Q-PSO) [14], biogeography optimization (BBO) [15], and hybrid differential evolution with BBO [16] have been utilized to solve the complex ELD problem considering valve point effects (VPE) and transmission losses (TL). Even though these techniques are the most fitting choices for nonlinear optimization, they inherently suffer from lower convergence rates, tendencies toward local minima, and are highly sensitive to the control parameters.

The methods used in the past provide reasonable solutions, but search efficiency drops and higher times for convergence are required when utilizing ELD with valve point effects [17–19]. Due to the above limitations, the hybridized techniques, such as Q-PSO [20], hybrid PSO (HPSO) [21], gravitational search algorithm (GSA) [22], enhanced multi–objective cultural algorithm (EMOCA) [23], improved orthogonal design PSO (IDPSO) [24], modified kill herd algorithm (MKHA) [25], modified crow search algorithm (MCSA) [26], a self-adapted across neighborhood search (SA-ANS) [27], flooding-based topology discovery algorithm (FBTDA) [28], JAYA with self-adaptive multi-population and levy flights (JAYA-SML) [29], JAYA with teaching learning-based optimization (JAYA-TLBO) [30], hybrid grey wolf optimization (HGWO) [31], kernel tricks (KSO) [32], an improved Q-PSO [33], emended salp swarm algorithm (ESSA) [34,35], exchange market algorithm method (EMAM) [36], peafowl optimization algorithm (POA) [37], and modified H-PSO with BAT algorithm-inspired acceleration coefficients (BAAC) [38] have been proposed in order to solve the ELD problem. The above algorithms do not always achieve the global best, but generally tend to reach near to the global optimal value [39,40]. The traditional static ELD problem seeks to minimize the generation cost of CFTGU for a certain load in a given time-period by satisfying limitations such as power balance and generation limits. Additionally, when the load demand fluctuates significantly, it becomes more challenging to solve the ELD problem due to the ramp rate constraints of the CFTGUs.

Another suitable actual power dispatch requirement is the DEELD, which uses the dynamic dispatching for a load cycle of a 24 h period. The DEELD problem has been tackled in a number of different ways to date. At first, mathematical methods such as lambda step, optimal point, participation coefficients, and gradient-based approaches have generally been utilized for the DEELD problem. However, mathematical methods have drawbacks such as excessive memory utilization and being less accurate when addressing a highly complex problem. As a result, numerous artificial intelligence techniques (AIT) have since been used to tackle the DEELD problem and produce successful dispatch outcomes. In this context, to solve the multi-objective DEELD (MO-DEELD) problem, the dynamic non-sorted biogeography-based optimization (Dy-NSBBO) algorithm is suggested in reference [41]. Similarly, the algorithms such as the multi-objective virus colony search (MO-VCS) algorithm [42], moth–flame optimization with position disturbance updating strategy (MFO-PDU) [43], improved tunicate swarm algorithm (ITSA) [44], and improved sailfish algorithm (ISFO) [45] were created in order to solve the DEELD problem in the recent past. In [46], the authors noted that the DEELD problem is more challenging address as it involves both fuel and pollution costs.

Similarly, in [47], an improved bacterial foraging algorithm (IBFA) was implemented in order to solve the DEELD problem. In [48], the DEELD problem was solved using a multi-objective BAT optimization algorithm, which considers slope rate constraints and valve point effects. In [49], the convergence performance was not confirmed when the orthogonal-PSO algorithm was implemented to solve the DEELD problem. Likewise, many works have not addressed the emissions objectives when attempting to solve the DEELD problem [50]. In sum, even though the previous algorithms have been successfully applied

to the DEELD problem, various drawbacks, such as higher convergence rates, a tendency to become stuck at local optimum values, and addressing only limited objectives, can be identified as major gaps.

On the other hand, the elephant herd optimization (EHO) algorithm has a strong potential of achieving a global optimal solution, with robustness and fast convergence speed; it is a newly proposed intelligent algorithm (see [51] and [52]). It has proven its ability to achieve the global optimal solution by implementing it in various standard test functions [53]. Likewise, the EHO has proven its ability to obtain the optimal solution using lower convergence rates when subjected to the design of the optimal PI controller for the control of the grid-tied four-phase switched reluctance generator (SFG) [54]. Furthermore, the discrete EHO (DEHO)-based partial transmit sequence (PTS) method is recommended to improve the peak-to-average power ratio of universal filtered multicarrier (UFMC) signals to minimum levels. The recent literature describing the static/dynamic ELD problem and a summary of the implemented algorithms are presented in Table 1.

Table 1. Literature review describing the methodology and associated problem of interest.

Reference	Methodology	Static ELD	Dynamic EELD
[4,5]	SQP	✓	✗
[7]	IGAMU	✓	✗
[8]	HDE	✓	✗
[9]	AP-PSO	✓	✗
[12]	ESO	✓	✗
[13]	ABC	✓	✗
[14,20]	Q-PSO	✓	✗
[15]	BBO	✓	✗
[16]	Hybrid-BBO	✓	✗
[21]	Hybrid-PSO	✓	✗
[22]	GSA	✓	✗
[23]	EMOCA	✓	✗
[24]	IDPSPO	✓	✗
[25]	MKHA	✓	✗
[26]	MCSA	✓	✗
[31]	HGWO	✓	✗
[34]	ESSA	✓	✗
[36]	EMAM	✓	✗
[41]	Dy-NSBBO	✗	✓
[42]	MO-VCS	✗	✓
[43]	MFO-PDU	✗	✓
[44]	ITSA	✗	✓
[45]	ISFO	✗	✓
[47]	IBFA	✓	✓
Proposed	EHO	✓	✓

1.2. Research Contributions

The major contributions of this work are as follows:

1. An artificial intelligence algorithm, namely, elephant herd optimization (EHO), is implemented in order to solve a critical engineering problem.

2. The algorithm is implemented in order to solve both the convex static and dynamic EELD problems of power systems.
3. The predictability of the proposed algorithm is evaluated by implementing the algorithm on three different systems, such as 6-, 10-, and 40-unit systems.
4. The obtained results are compared to the recent available algorithms in the literature to demonstrate the efficacy of the proposed approach.

1.3. Organization of the Present Work

Section 2 outlines the basic ELD problem formulations with various constraint scenarios. Section 3 illustrates the modeling of DEELD problem with constraints. Section 4 discusses the mathematical modeling of the EHO algorithm. Finally, Section 5 deliberates on the results, and Section 6 presents the conclusions drawn from the present work.

2. Problem Formulation for the Basic ELD Problem

2.1. Objective Function

The basic ELD problem comprises a fitness function along with various practical constraints. In the basic form, the fitness function is a quadratic function that describes the various cost functions of participating generators [20] on a hourly basis. The mathematical form of the fitness function for the BELD problem is shown below:

$$F_{BELD} = \sum F_g(P_g) = \sum a_g P_g^2 + b_g P_g + c_g \ \$/\text{h} \quad \forall g \in N_g \tag{1}$$

The ELD problem consists of minimizing F_{BELD} is subject to the following constraints.

2.2. Constraints

2.2.1. Power Balance Constraints

The total power generated should be equal to the sum of the total load on the system and total transmission line network losses [25]. The mathematical form for the power balance constraint is shown below:

$$\sum_g P_g - \sum_d P_d - P_L = 0 \quad \forall g \in N_g \text{ and } \forall d \in N_d \tag{2}$$

The transmission loss P_L may be represented using B coefficients [39]:

$$P_L = \sum_g \sum_g [P_g][B][P_g] + \sum_g B_0 P_g + B_{00} \quad \forall g \in N_g \tag{3}$$

2.2.2. Generator Capacity Constraints

The output delivered from the generators maintained to be within their lower and upper limits, as shown below:

$$P_g^{min} \le P_g \le P_g^{max} \quad \forall g \in N_g \tag{4}$$

2.2.3. Ramp Rate Limits Constraints

The power delivered P_g by the generator g in a period is to be maintained within certain up-ramp UR_g and down-ramp DR_g limits [34], with respect to the previous P_{g0}. This is shown below:

$$P_g - P_{g0} \le UR_g \quad \text{if } P_g \ge P_{g0} \quad \forall g \in N_g \tag{5}$$

and

$$P_{g0} - P_g \le DR_g \quad \text{if } P_g \le P_{g0} \quad \forall g \in N_g \tag{6}$$

and

$$\text{Max}\left(P_g^{min}, P_{g0} - DR_g\right) \le P_g \le \text{Min}\left(P_g^{max}, P_{g0} + UR_g\right) \quad \forall g \in N_g \tag{7}$$

The fitness function (1) is subject to real power balance constraints (2), generator capacity constraints (4), and ramp rate limit constraints (7).

3. Problem Formulation for Dynamic EELD Problem

In this section, we provide the mathematical formulations for the DEELD problem. We assume that the network has dispatchable power generators, $\forall g \in N_g$. The control variables of the DEELD problem are collected in the vector at each hour $x = [x_1, x_2, \ldots x_n]$, where $\{x \in P_g \forall g\}$ and P_g is the vector collecting the generations for all $\forall g \in N_g$. Let the function $f_{DEED} : \mathbb{R} \to \mathbb{R}$ be the positive valued, differentiable, non-decreasing, and convex objective function that captures the generation cost for the DEELD problem. Let the $\partial_{P_g}(f_{DEELD})$ be the partial derivative with respective to the control variable P_g and the constraints imply that $\partial_{P_g}(f_{DEELD}) \geq 0$ for all $\forall g \in N_g$ [49]. The cost function for the DEELD problem f_{DEED} comprises a fuel cost function f_{FCF} and an emission dispatch function f_{EDF}, which are shown as follows:

3.1. Fuel Cost Function

The 24 h fuel cost function for all $\forall g \in N_g$ is represented as quadratic costs valued in USD (\$) [48]. The fuel cost function utilized in this work is shown as below:

$$f_{FCF} = \sum_{t=1}^{N_H} \sum_{g=1}^{N_g} a_g P_{g,t}^2 + b_g P_{g,t} + c_g \$ \quad \forall g \in N_g, \forall t \in N_H \tag{8}$$

3.2. Emission Dispatch Function

The next fitness function is the emission pollutants (f_{EDF}) in (kgs). It has a straight relationship with the output generated from the gth conventional generator. The emissions include CO_2, nitrogen oxide (NOx) and sulfur oxide (SOx), which are caused by the burning of fossil fuels [48]. The f_{EDF} can be expressed as follows:

$$f_{EDF} = \sum_{t=1}^{N_H} \sum_{g=1}^{N_g} \alpha_g P_{g,t}^2 + \beta_g P_{g,t} + \gamma_g \quad \forall g \in N_g, \forall t \in N_H \tag{9}$$

The above functions are minimized, as they are subject to various constraints, i.e., limits on active power generations, ramp rate limits, power balance constraints, and transmission loss constraints. The next sub-section discloses the constraints considered in this work.

3.3. Constraints

Transmission losses: The loss at any time segment tth, including B-coefficients, is given as follows:

$$P_{loss,t} = \sum_{i=1}^{N_g} \sum_{j=1}^{N_g} [P_{i,t}] \times [B] \times [P_{j,t}] + \sum_{g=1}^{N_g} B_0 \times P_{g,t} + B_{00} \quad \forall g \in N_g, \forall t \in N_H \tag{10}$$

Active Power Balance Constraints: The power generated at any tth time segment is utilized to supply the demand and transmission losses at the given time segment. This is mathematically represented as follows:

$$\sum_{g=}^{N_g} P_{g,t} = P_{d,t} + P_{loss,t} \quad \forall g \in N_g, \forall t \in N_H \tag{11}$$

Limits on active power generation: The active power generation $P_{g,t}$ at time segment t is restricted by the prescribed upper and lower limits. Figure 1 shows the pictorial representation of the maximum and minimum limits of a 6-unit system. This is mathematically represented as follows:

$$P_g^{min} \leq P_{g,t} \leq P_g^{max} \quad \forall g \in N_g, \forall t \in N_H \tag{12}$$
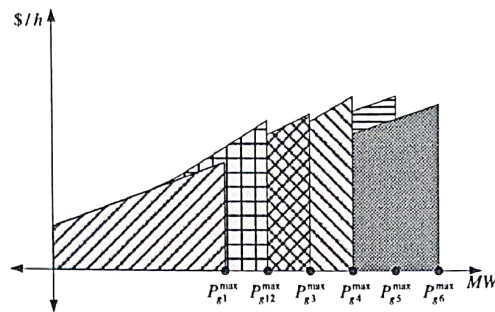
Figure 1. Thermal generator maximum and minimum limits.

Ramp Rate Limits: This is specified as follows [45]:

$$P_{g,t-1} - P_{g,t} \leq UR_g \quad \text{if } P_{g,t} \geq P_{g,t-1} \quad \forall g \in N_g, \forall t \in N_H \tag{13}$$

$$P_{g,t-1} - P_{g,t} \leq DR_g \quad \text{if } P_{g,t} \leq P_{g,t-1} \quad \forall g \in N_g, \forall t \in N_H \tag{14}$$

$$max\left(P_g^{min}, P_{g,t-1} - DR_g\right) \leq P_{g,t} \leq min\left(P_g^{max}, P_{g,t-1} + UR_g\right) \quad \forall g \in N_g, \forall t \in N_H \tag{15}$$

3.4. Weighted Fitness Function to Obtain the Optimal Scheduling Strategy

The weighted fitness function has been utilized in order to find the optimum fuel cost and emission dispatch of the generators. The weighted multi-objective function is discussed as follows:

$$f_T = u_1 f_{FCF} + u_2 f_{EDF} \tag{16}$$

where u_1 and u_2 are the weighting factors, set as 0.5 in this work.

Constraint Handling

The power balance constraints, including the real power generations, load demand, and charging/discharging, are handled by including a penalty factor to the objective function (17) as shown below:

$$Pf_T = u_1 f_{FCF} + u_2 f_{EDF} + \lambda_1 \left[\sum_{g=1}^{N_g} P_{g,t} - P_{d,t} - P_{loss,t}\right] + \lambda_2 \sum_{g=1}^{N_{gb}} \Delta P_g^2 + \lambda_3 \sum_{rg=1}^{N_{rb}} \Delta P_{rg}^2 \tag{17}$$

where

$$\Delta P_g = \begin{cases} P_g^{min} - P_{g,t} & \text{if } P_{g,t} \leq P_g^{min} \\ P_g^{max} - P_{g,t} & \text{if } P_{g,t} \geq P_g^{max} \end{cases} \tag{18}$$

$$\Delta P_{rg} = \begin{cases} P_{g,t-1} - P_g \leq UR_g & \text{if } P_g \leq P_g^{min} \\ P_{g,t-1} - P_g \leq DR_g & \text{if } P_g \geq P_g^{max} \end{cases} \tag{19}$$

The fitness function (17) is subjected to real power balance constraints (10), limits on active power generation (11), and ramp rate limits specified in (13)–(15).

4. Elephant Herd Optimization

In 2015, Wang et al. [51] created the EHO algorithm, taking inspiration from the social behaviors of elephant herds observed in nature. Even though elephants demonstrate intelligent behavior in real life, the EHO algorithm was created using the following idealized rules. The elephant population is divided into clans containing a constant number of elephants in each clan. One elephant in each tribe guides the others as they look for food and water. Additionally, as generations pass, some elephants of a particular age leave their clan to live independently in distant areas far from the family group they belong to. On this

basis, the basic EHO algorithm is designed to have two main phases, namely clan updating and separation.

Clan Updating Operator

As previously stated, each of the elephants is led by a matriarch in their respective clan. Thus, matriarch authority ci influences the next position of each elephant in the clan ci. For instance, elephant j in clan ci is updated as follows:

$$x_{new,ci,j} = x_{ci,j} + \alpha \times \left(x_{best,ci} - x_{ci,j}\right) \times r \tag{20}$$

Here, uniform conveyance is utilized. No group's fittest elephant can be replenished by Equation (18). For the finest elephant, the clan is updated as shown below:

$$x_{new,ci,j} = \beta \times x_{centre,ci} \tag{21}$$

We can observe a new individual, $x_{new,ci,j}$, in Equation (19), which is produced by the data obtained by all the elephants in the clan ci. $x_{centre,ci}$ for the dth aspect may be calculated as follows:

$$x_{centre,ci,d} = \frac{1}{n_{ci}} \times ci \sum_{j=1}^{n_{ci}} x_{ci,j,d} \tag{22}$$

The center of clan $ci, x_{centre,ci,d}$ can be determined through the D estimations using Equation (20). Using the process above, the group refreshing administrator can be uncovered. When they reach puberty, the male elephants in each clan will depart from their group and live independently. When handling improvement-related concerns, an administrator can serve as an example of this isolating cycle. Let us assume that the elephants with the worst health will act as the isolating administrator at every age in order to improve the search capability of the EHO strategy. This mechanism is shown in Equation (21).

$$x_{worst,ci} = x_{min} + (x_{max} - x_{min} + 1) \times rand \tag{23}$$

The pseudo-codes for the clan updating operator and separating operator are shown in Figure 2 below.

Pseudo code for clan updating operator

Begin

for ci = 1 to n_{ci} do, for j = 1 to n_j do

  Update $x_{ci,j}$ and generate according to Equation (15).

if $x_{ci,j} = x_{best,ci}$ then

  Update $x_{ci,j}$ and generate $x_{new,ci,j}$ according to Equation (16)

end if, end for j, end for ci,

end

Pseudo code for separating operator

Begin

for ci = 1 to n_{ci} do

  Replace the worst elephant individual in clan ci by Equation (20).

end for ci

end

Figure 2. Pseudo-codes for the EHO algorithm.

5. Case Study

5.1. Description of Systems

In this study, the EHO algorithm is used to minimize the total fuel cost for both static and dynamic ELD problems of the power system. The results are evaluated on three different test systems to assess the effectiveness of the proposed approach. Concisely, the flow chart in Figure 3 illustrates the internal mechanism of the proposed algorithm along with process of achieving results.
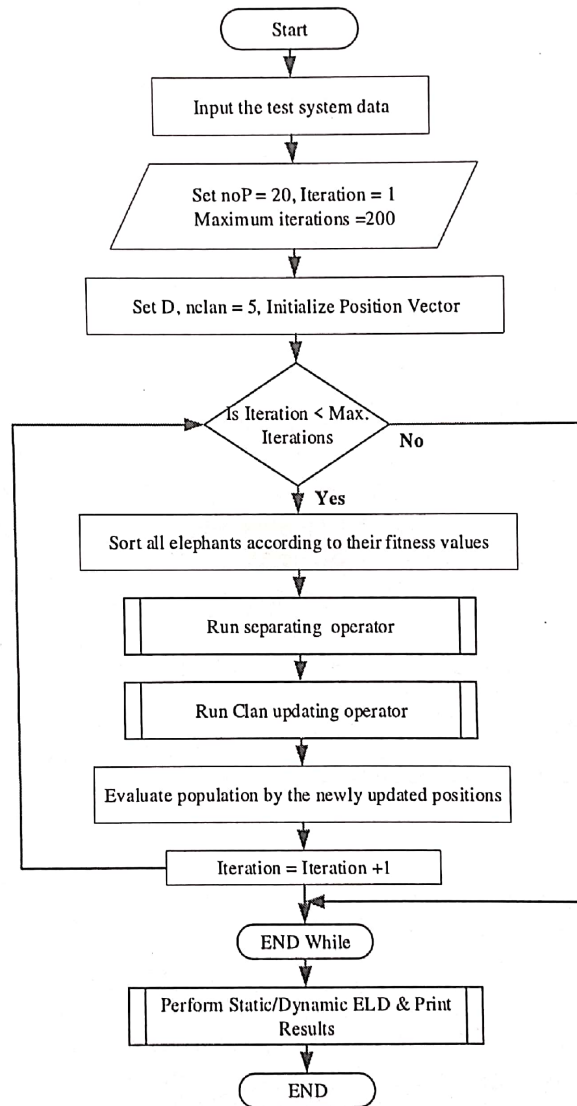

Figure 3. Flow chart for proposed EHO algorithm for ELD/DEELD problems.

5.1.1. Test System 1

Test system 1 utilized in the present study is a six-unit system. The details such as generator cost coefficients, generator limits, and the loss matrix of the test system 1 are shown in Table 2 below, which are taken from reference [25].

Table 2. Data for the six-unit system.

i	P_{gi}^{max}	P_{gi}^{min}	a_{gi}	b_{gi}	c_{gi}	B_{1i}	B_{2i}	B_{3i}	B_{4i}	B_{5i}	B_{6i}
1	500	100	0.007	7	240	0.002022	−0.000286	−0.000534	−0.000565	−0.000454	−0.000103
2	200	50	0.0095	10	200	−0.000286	0.003243	0.000016	−0.000307	−0.000422	−0.000147
3	300	80	0.009	8.5	220	−0.000533	0.000016	0.002805	0.000831	0.000023	−0.000270
4	150	50	0.009	11	200	−0.000565	−0.000307	0.000831	0.001129	0.000113	−0.000295
5	200	50	0.008	10.5	220	−0.000454	−0.000422	0.000023	0.000113	0.000460	−0.000153
6	120	50	0.0075	12	190	0.000103	−0.000147	−0.000270	−0.000295	−0.000153	0.000898

5.1.2. Test System 2

Similarly, in this study, test system 2 is a 40-unit system. The details related to this system are taken from references [30,32].

5.1.3. Test System 3

Similarly, in this study, test system 3 is a 10-unit system. The details related to this system are taken from reference [50].

5.2. Parameter Setting and System Configurations

The proposed EHO algorithm for solving static/dynamic ELD problems was implemented using MATLAB on a 64-bit laptop with a 2.60 GHz CPU and 8 GB RAM. Meanwhile, to evaluate their effectiveness, the results obtained from the proposed EHO algorithm at every stage are compared with standard algorithms, such as BAT [55], ALO [56], and those from other recently published works. The algorithm was tested on each test system 20 times to minimize the statistical errors, and the obtained results were compared with the previous literature. Further, the weighting factors, such as u_1 and u_2 in (17), are set to 0.5 in order to provide the equal preferences for the considered objectives [57]. Before proceeding to the simulated calculation, the careful selection of parameter settings is important to produce a competent result. The selection of the parameters, such as $iter_{max}$, considerably affects the performance of the EHO in terms of the present problem of interest. To successfully implement the EHO, the values of $iter_{max}$ were varied, namely as 100, 200, and 500 in order to obtain the best parameter setting. The results of this are presented in Table 3 for test system 1. Based on the results from Table 3, it can be observed that the EHO algorithm provides the best results when $iter_{max} = 200$ for test system 1.

Table 3. Parameter setting of EHO algorithm for test system 1.

$iter_{max}$	Best Cost (USD)	Worst Cost (USD)	Average Cost (USD)	Standard Deviations
100	15,299.62	15,428.46	15,339.83	34.78751
200	15,286.47	15,349.92	15,315.31	17.00265
500	15,293.25	15,351.38	15,308.31	15.80449

5.3. Computation Results and Comparisons
5.3.1. Test System 1

In this case, a six-unit static ELD problem considering losses is used to test the effectiveness of the proposed EHO algorithm. A general load demand $\sum P_d$ of 1263 MW is considered in the present test case. Twenty trials were utilized to evaluate each algorithm and the results were analyzed based on the best, worst, and standard deviation values obtained. Based on the static results obtained in Table 3 and to validate these, the $iter_{max}$ was set to 200 for the proposed EHO, ALO, and BAT algorithms, as shown in Table 4. The optimization results of the proposed and other reported approaches are shown in Table 5. The best fuel cost in this case is achieved through the EHO algorithm at 15,286.47 (USD/h), which is low compared to 15,443.0 (USD/h), 15,796.02746 (USD/h), and 15,814.97355 (USD/h) achieved by MKHA, ALO, and BAT algorithms, respectively. It is also clear from Table 5 that the proposed EHO algorithm provides a much better solution

with less computational time compared to MKHA, ALO, and BAT algorithms. Furthermore, the convergence curves obtained by the proposed EHO and other reported approaches are shown in Figure 4. It can be observed that the EHO algorithm converges at a low number of iterations, which reinforces the superiority of the proposed approach. In addition, the results have been evaluated and validated using a medium-sized test bus system.

Table 4. Parameters considered for the reported algorithms.

Algorithm	$iter_{max}$	noP	Others	Reference
ALO	200	20	Not Reported	[56]
BAT	200	20	$\alpha = 0.99, \gamma = 0.9$	[58]
EHO	200	20	nClan = 5	Proposed Work

Table 5. Comparative results of the six-unit system with $\sum P_d = 1263$ MW.

| i/Parameter	EHO	MKHA [25]	ALO [56]	BAT [58]
P_{g1}(MW)	439.858	447.3998	473.84	499.9837
P_{g2}(MW)	185.133	173.2424	181.75	148.8036
P_{g3}(MW)	247.6364	263.3833	265.87	270.8342
P_{g4}(MW)	133.7811	138.9778	129.85	127.1789
P_{g5}(MW)	160.6319	165.3929	165.35	179.3078
P_{g6}(MW)	96.18851	87.0495	85.081	75.5512
$\sum P_{gi}$(MW)	1263.229	1275.44	1301.74	1301.659
Losses (MW)	0.229	12.44	38.74	38.659
Best Cost (USD)	15,286.47	15,443.00	15,796.02746	15,814.97355
Worst Cost (USD)	15,349.92	15,443.00	15,796.02746	15,898.4937
Standard Deviations	17.00265	0.2318	7.46498×10^{-12}	23.83492754
Average Cost (USD)	15,315.31	15,443.00	15,796.02746	15,839.77276
CPU Time (secs)	2.29	7.41	2.46	2.72
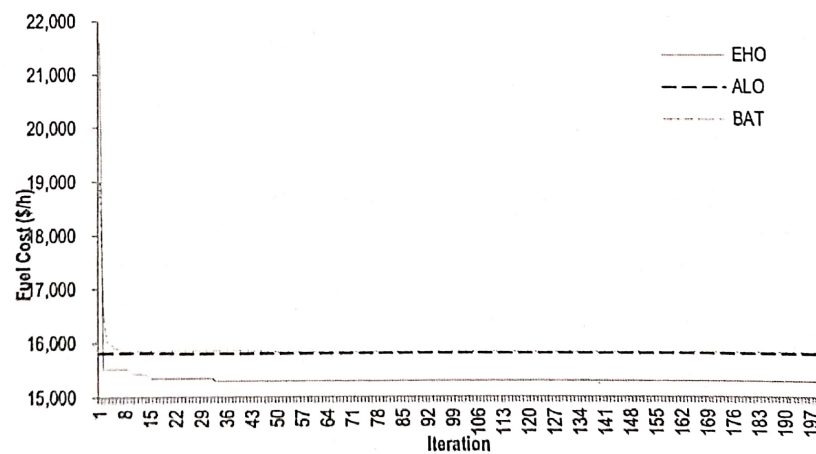
Figure 4. Convergence curve for various algorithms for a six-unit system with $\sum P_d = 1263$ MW.

5.3.2. Test System 2

This case study consists of 40 generators, meeting a demand of $\sum P_d = 10,500$ MW. The optimal scheduling of the generators in this case by the EHO, ALO, and BAT algorithms is shown in Figure 5. Similarly, the results obtained in this case by the EHO algorithm are compared with recent similar approaches, such as KSO [32], HDE [8], Beta-HC-GWO [59], and CBPSO-RVM [21], and are shown in Table 6. From the comparisons shown in Table 6, it can be seen that, among the reported algorithms such as BAT, ALO, and EHO, EHO performs well in respect to fuel costs. Furthermore, amongst all other algorithms listed, EHO performs better while producing minimum fuel costs as well as time consumptions. The convergence curves for the algorithms EHO, BAT, and ALO are shown in Figure 6. The

micro-level examination of the figure reveals that the proposed EHO algorithm converges in the early stage (before 80 iterations), while the other two only settled with difficulty. The results demonstrate the superiority and practicability of the proposed EHO over the large test systems. Furthermore, to confirm the feasibility of the proposed EHO algorithm, the problem involving a dynamically varying load is discussed in the next section.
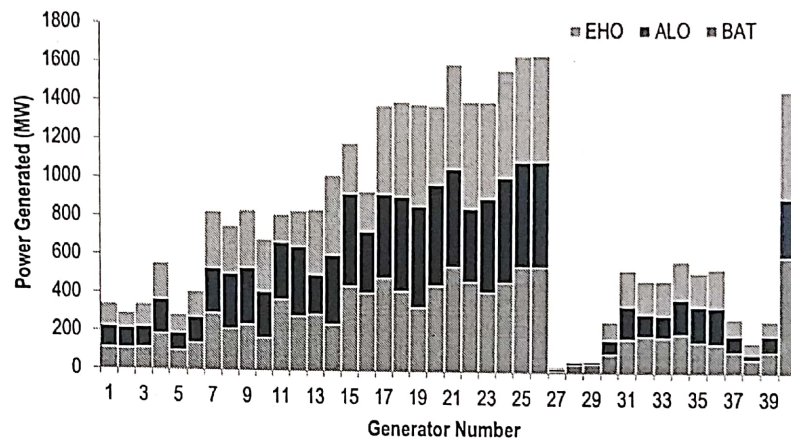

Figure 5. Active power generation of a 40-unit system with $\sum P_d = 10,500$ MW.

Table 6. Comparative results of a 40-unit system with $\sum P_d = 10,500$ MW.

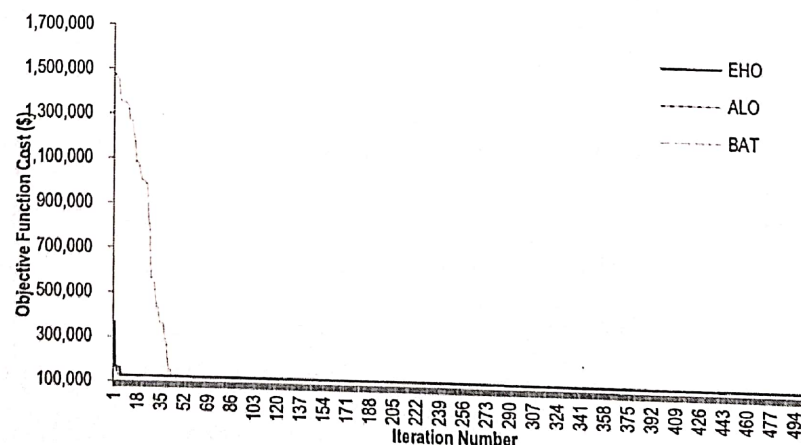| Method	Best Cost (USD)	Time Consumption
BAT	124,835.00	21.0129
ALO	124,229.97	27.5294
KSO [32]	125,491.00	Not Reported
Self Turing HDE [8]	123,496.02	16.86025
Beta-HC-GWO (0.5) [59]	123,162.04	Not Reported
CBPSO-RVM [21]	122,281.14	Not Reported
EHO	121,478.96	21.2882

Figure 6. Convergence curve for various algorithms for a 40-unit system with $\sum P_d = 10,500$ MW.

5.3.3. Test Case 3

In this case, a 10-unit DEELD problem is used to evaluate the 24 h period fuel cost utilizing the proposed EHO algorithm. The data-related costs and up/down limits of the 10-unit system are taken from [24]. The general load profile referred to by most recent works such as [48] and [49] is depicted in Figure 7 below. Here also, in order to obtain the best setting of $iter_{max}$, $iter_{max}$ has been varied as 100, 200 and 500. The results of this are presented

in Table 7 for test system 2. Based on the results from Table 6, it can be observed that the EHO algorithm provides the best results when the $iter_{max} = 500$ (as in test system 2).
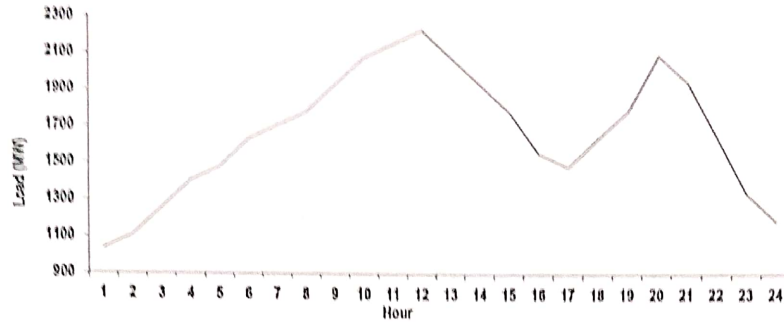

Figure 7. Load profile for a 10-unit system.

Table 7. Parameter setting of EHO algorithm for test system 3.

$iter_{max}$	Best Cost (USD)	Worst Cost (USD)	Average Cost (USD)	Standard Deviations
100	1,019,633.2	1,042,786.93	10,357,443.29	789.6
200	1,018,657.22	1,036,723.74	1,024,656.78	742.86
500	1,013,950.00	1,019,502.00	10,301,860.00	889.1759

The optimal dispatch of the 10-unit system in a period of 24 h by the proposed EHO algorithm is shown in Figure 8. The results, such as fuel costs and emissions on an hourly basis, are depicted in Table 8. It can be observed that the total fuel costs, f_{FCF}, and total emissions, f_{EDF}, for a period of 24 h, obtained by the proposed EHO algorithm, are 1,013,950 (USD) and 648,085 (kg) respectively. Furthermore, the comparative analysis of the obtained results with those of the previous benchmark approaches, such as ICA [60], CDE [61], DE [62], AIS [63], ECE [64], IPSO [65], DGPSO [66], BAT, ALO, SOA-SQP [67], PSO-SQP [68], MHEP-SQP [69], AIS-SQP [70], and CS-DE [71] algorithms, are shown in Table 9. From the table, it can be declared that the proposed EHO algorithm outperforms the previous approaches. In addition, the convergence characteristics of the proposed EHO and other reported approaches, such as ALO and BAT, are shown in Figure 9. From the figure, it can be seen that the proposed approach converges in a smaller number of iterations, as compared to other reported approaches. The comprehensive result analysis also demonstrates that the proposed approach has a remarkable impact on both static and dynamic EELD problems.
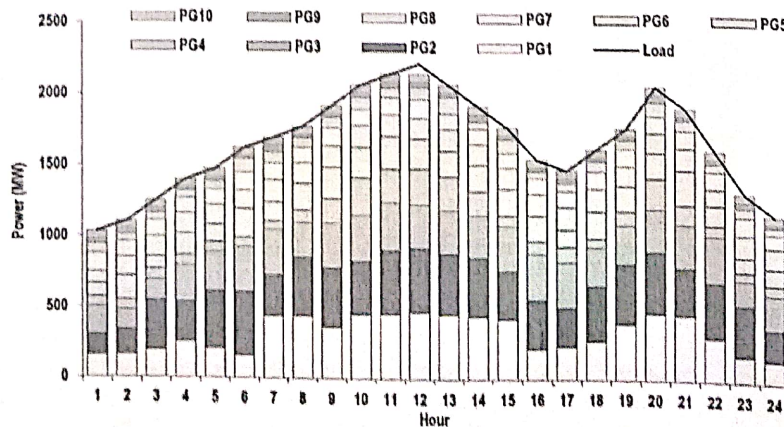

Figure 8. Hourly generation and the corresponding load of DEED problem via the EHO algorithm.

Table 8. Cost-based results for test system 3.

t	$f_{FCF,t}$	$f_{EDF,t}$	t	$f_{FCF,t}$	$f_{EDF,t}$
1	28,466	22,085	13	51,341	30,031
2	30,231	23,954	14	47,737	30,462
3	33,190	22,353	15	44,481	26,528
4	36,406	25,311	16	39,467	24,031
5	38,248	29,537	17	38,078	26,984
6	41,081	24,784	18	41,240	23,879
7	42,784	27,220	19	44,597	25,721
8	44,425	28,461	20	51,694	30,470
9	47,801	28,854	21	47,638	27,604
10	51,476	31,531	22	41,236	25,644
11	53,038	31,366	23	34,649	23,745
12	53,079	33,799	24	31,567	23,731
			Total	1,013,950	648,085

Table 9. Comparative results of a 10-unit system with dynamic loading.

| Method	Best Cost (USD)	Average Cost (USD)	Worst Cost (USD)	Standard Deviation
		Individual approaches		
ICA [60]	1,018,467.49	1,019,291.358	1,021,795.773	687.56
CDE [61]	1,019,123.00	1,020,870.00	1,023,115.00	-
DE [62]	1,019,786.00	-	-	-
AIS [63]	1,021,980.00	1,023,156.00	1,024,173.00	-
ECE [64]	1,022,271.58	1,023,334.93	-	-
IPSO [65]	1,023,807.00	1,026,863.00	-	-
DGPSO [66]	1,028,835.00	1,030,183.00	-	-
BAT	1,033,416.00	-	-	-
ALO	1,035,431.00	-	-	-
		Hybrid approaches		
SOA-SQP [67]	1,021,460.00	-	-	-
PSO-SQP [68]	1,027,334.00	1,028,546.00	-	-
MHEP-SQP [69]	1,028,924.00	1,021,179.00	-	-
AIS-SQP [70]	1,029,900.00	-	-	-
CS-DE [71]	1,023,432.00	1,026,475.00	1,027,634.00	-
Proposed EHO	1,013,950.00	1,019,502.00	10,301,860.00	889.1759
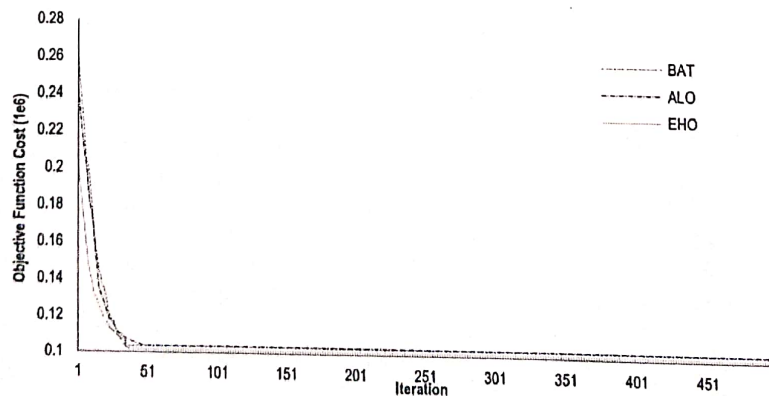
Figure 9. Convergence curve for various algorithms for the 10-unit system DEED problem.

6. Conclusions

In this study, a novel EHO method was used to resolve the power system's static and dynamic EELD problems. For both small- and large-scale test systems, the performance of the EHO algorithm was investigated in a variety of instances, involving both the static ELD

and dynamic EELD problems. The numerical simulation demonstrates that the suggested EHO method is capable of finding the best scheduling for the test systems in regard to static and dynamic EELD problems. The comparative analysis of the fuel cost function value obtained by the EHO algorithm, with respect to the BAT and ALO algorithms, demonstrates its superiority and could save billions of USD annually by making the generating units eco-friendlier.

Furthermore, the convergence results also demonstrate that the proposed approach provides a significant reduction in fuel costs and convergence time for both small- and large-scale test systems, while solving complicated optimization problems in power systems. Finally, it can be concluded that the proposed approach is a superior alternative for power system operators to obtain an improved dispatch schedule for static and dynamic EELD problems in small- and large-scale systems, irrespective of their complexities.

Author Contributions: Conceptualization, R.P., Y.K.N. and S.R.S.; methodology, S.K.W., R.P. and S.R.S.; software, R.P. and S.K.W.; validation, R.P., Y.K.N. and S.R.S.; formal analysis, Y.K.N., S.K.W.; investigation, R.P., S.K.W. and S.R.S.; resources, R.P. and S.R.S.; data curation, R.P. and S.R.S.; writing—original draft preparation, R.P. and S.K.W.; writing—review and editing, R.P., S.K.W. and S.R.S.; visualization, R.P. and Y.K.N.; supervision, R.P., S.K.W. and S.R.S.; project administration, Y.K.N. and S.K.W.; funding acquisition, R.P. and S.R.S. All authors have read and agreed to the published version of the manuscript.

Data Availability Statement: The data used to support the findings of this study are publicly available online, and any further information required is available from the corresponding author upon request.

Conflicts of Interest: The authors declare no conflict of interest.

Nomenclature

$F_g(P_g)$	The quadratic cost function of gth generator in ($/h)
a_g, b_g and c_g	The cost coefficients of the gth generator in $\left(\$/\text{MW}^2\text{h}\right)$
P_g	The active power output from the gth generator in MW
N_g	The total number of CFTGU
P_d	The power demand at the dth load in MW
$[B], B_0, B_{00}$	The loss coefficient matrices
P_g^{max}	Maximum limit of active power generation of gth generator
P_g^{min}	Minimum limit of active power generation of gth generator
$x_{new,ci,j}$	Recently refreshed for elephant$j$ in clan ci
$x_{ci,j}$	Recently refreshed for elephant$j$ in clan ci
$x_{best,ci}$	Matriarch ci which is the fittest elephant individual in clan ci
r	Random value between [0, 1]
β	Random value between [0, 1]
D	Total dimension
n_{ci}	Quantity of elephants in ci clan
$x_{ci,j,d}$	The dth elephant individual of $x_{ci,j}$
x_{max}	The upper bound of the position of elephant individual
x_{min}	The lower bound of the position of elephant individual
$x_{worst,ci}$	Worst elephant individual in clan ci
$x_{centre,ci}$	Centre of clan ci
$rand \in [0,1]$	A real between the range [0 1]

Acronyms

GHGs	Greenhouse Gases
ELD	Economic Load Dispatch
DEELD	Dynamic Economic Emission Load Dispatch
EHO	Elephant Herd Optimization
CFTGU	Coal-Fired Thermal Generating Unit
VPE	Valve Point Effects
PTS	Partial Transmit Sequence
SFG	Switched Reluctance Generator
UFMC	Universal Filtered Multicarrier
GA	Genetic Algorithm
EP	Evolutionary Programming
SQP	Sequential Quadratic Programming
PSO	Particle Swarm Optimization
TL	Transmission Losses
IGAMU	Improved Genetic Algorithm with Multiplier Updating
HDE	Self-Tuning Hybrid Differential Algorithm
AP-PSO	Anti-Predatory PSO
ESO	Evolutionary Strategy Optimization
Q-PSO	Quantum Mechanics Inspired PSO
BBO	Biogeography Optimization
HPSO	Hybrid PSO
GSA	Gravitational Search Algorithm
EMOCA	Enhanced Multi-Objective Cultural Algorithm
IDPSO	Improved Orthogonal Design PSO
MKHA	Modified Kill Herd Algorithm
MCSA	Modified Crow Search Algorithm
SA-ANS	Self-Adapted Across Neighborhood Search
FBTDA	Flooding Based Topology Discovery Algorithm
HGWO	Hybrid Grey Wolf Optimization
ESSA	Emended Salp Swarm Algorithm
EMAM	Exchange Market Algorithm Method
POA	Peafowl Optimization Algorithm
Dy-NSBBO	Dynamic Non-Sorted Biogeography-Based Optimization
MO-VCS	Multi-Objective Virus Colony Search
MFO-PDU	Moth–Flame Optimization with Position Disturbance Updating Strategy
ITSA	Improved Tunicate Swarm Algorithm
ISFO	Improved Sailfish Algorithm
IBFA	Improved Bacterial Foraging Algorithm

References

1. Wu, M.; He, Q.; Liu, Y.; Zhang, Z.; Shi, Z.; He, Y. Machine Learning Techniques for Decarbonizing and Managing Renewable Energy Grids. *Sustainability* 2022, *14*, 13939. [CrossRef]
2. Mei, P.; Wu, L.; Zhang, H.; Liu, Z. A Hybrid Multi-Objective Crisscross Optimization for Dynamic Economic/Emission Dispatch Considering Plug-In Electric Vehicles Penetration. *Energies* 2019, *12*, 3847. [CrossRef]
3. Montoya, O.D.; Gil-González, W.; Grisales-Noreña, L.F. An Exact MINLP Model for Optimal Location and Sizing of DGs in Distribution Networks: A General Algebraic Modeling System Approach. *Ain. Shams. Eng. J.* 2019, *11*, 409–418. [CrossRef]
4. Subathra, M.S.P.; Easter Selvan, S.; Aruldoss Albert Victoire, T.; Hepzibah Christinal, A.; Amato, U. A Hybrid with Cross-Entropy Method and Sequential Quadratic Programming to Solve Economic Load Dispatch Problem. *IEEE Syst. J.* 2015, *9*, 1031–1044. [CrossRef]
5. Jabr, R.A. Solution to Economic Dispatching with Disjoint Feasible Regions via Semidefinite Programming. *IEEE Trans. Power Syst.* 2012, *27*, 572–573. [CrossRef]
6. Sailesh Babu, G.S.; Bhagwan Das, D.; Patvardhan, C. Real-Parameter Quantum Evolutionary Algorithm for Economic Load Dispatch. *IET Gener. Transm. Distrib.* 2008, *2*, 22–31. [CrossRef]
7. Chiang, C.L. Genetic-Based Algorithm for Power Economic Load Dispatch. *IET Gener. Transm. Distrib.* 2007, *1*, 261–269. [CrossRef]
8. Wang, S.K.; Chiou, J.P.; Liu, C.W. Non-Smooth/Non-Convex Economic Dispatch by a Novel Hybrid Differential Evolution Algorithm. *IET Gener. Transm. Distrib.* 2007, *1*, 793–803. [CrossRef]

9. Selvakumar, A.I.; Thanushkodi, K. Anti-Predatory Particle Swarm Optimization: Solution to Nonconvex Economic Dispatch Problems. *Electr. Power Syst. Res.* 2008, 78, 2–10. [CrossRef]

10. Sinha, N.; Chakrabarti, R.; Chattopadhyay, P.K. Evolutionary Programming Techniques for Economic Load Dispatch. *IEEE Trans. Evol. Comput.* 2003, 7, 83–94. [CrossRef]

11. Gaing, Z.L. Particle Swarm Optimization to Solving the Economic Dispatch Considering the Generator Constraints. *IEEE Trans. Power Syst.* 2003, 18, 1187–1195. [CrossRef]

12. Pereira-Neto, A.; Unsihuay, C.; Saavedra, O.R. Efficient Evolutionary Strategy Optimisation Procedure to Solve the Nonconvex Economic Dispatch Problem with Generator Constraints. *IEE Proc. Gener. Transm. Distrib.* 2005, 152, 653. [CrossRef]

13. Hemamalini, S.; Simon, S.P. Artificial Bee Colony Algorithm for Economic Load Dispatch Problem with Non-Smooth Cost Functions. *Electr. Power Compon. Syst.* 2010, 38, 786–803. [CrossRef]

14. Meng, K.; Wang, H.G.; Dong, Z.Y.; Wong, K.P. Quantum-Inspired Particle Swarm Optimization for Valve-Point Economic Load Dispatch. *IEEE Trans. Power Syst.* 2010, 25, 215–222. [CrossRef]

15. Bhattacharya, A.; Chattopadhyay, P.K. Biogeography-Based Optimization for Different Economic Load Dispatch Problems. *IEEE Trans. Power Syst.* 2010, 25, 1064–1077. [CrossRef]

16. Bhattacharya, A.; Chattopadhyay, P.K. Hybrid Differential Evolution with Biogeography-Based Optimization for Solution of Economic Load Dispatch. *IEEE Trans. Power Syst.* 2010, 25, 1955–1964. [CrossRef]

17. Li, L.; He, D.; Jin, J.; Yu, B.; Gao, X. Multi-Objective Load Dispatch Control of Biomass Heat and Power Cogeneration Based on Economic Model Predictive Control. *Energies* 2021, 14, 762. [CrossRef]

18. Tao, S.; Zhang, Y.; Yuan, M.; Zhang, R.; Xu, Z.; Sun, Y. Behavioral Economics Optimized Renewable Power Grid: A Case Study of Household Energy Storage. *Energies* 2021, 14, 4154. [CrossRef]

19. Mahdy, A.; El-Sehiemy, R.; Shaheen, A.; Ginidi, A.; Elbarbary, Z.M.S. An Improved Artificial Ecosystem Algorithm for Economic Dispatch with Combined Heat and Power Units. *Appl. Sci.* 2022, 12, 1773. [CrossRef]

20. Chakraborty, S.; Senjyu, T.; Yona, A.; Saber, A.Y.; Funabashi, T. Solving Economic Load Dispatch Problem with Valve-Point Effects Using a Hybrid Quantum Mechanics Inspired Particle Swarm Optimisation. *IET Gener. Transm. Distrib.* 2011, 5, 1042–1052. [CrossRef]

21. Lu, H.; Sriyanyong, P.; Song, Y.H.; Dillon, T. Experimental Study of a New Hybrid PSO with Mutation for Economic Dispatch with Non-Smooth Cost Function. *Int. J. Electr. Power Energy Syst.* 2010, 32, 921–935. [CrossRef]

22. Güvenç, U.; Sönmez, Y.; Duman, S.; Yörükeren, N. Combined Economic and Emission Dispatch Solution Using Gravitational Search Algorithm. *Sci. Iran.* 2012, 19, 1754–1762. [CrossRef]

23. Zhang, R.; Zhou, J.; Mo, L.; Ouyang, S.; Liao, X. Economic Environmental Dispatch Using an Enhanced Multi-Objective Cultural Algorithm. *Electr. Power Syst. Res.* 2013, 99, 18–29. [CrossRef]

24. Qin, Q.; Cheng, S.; Chu, X.; Lei, X.; Shi, Y. Solving Non-Convex/Non-Smooth Economic Load Dispatch Problems via an Enhanced Particle Swarm Optimization. *Appl. Soft Comput. J.* 2017, 59, 229–242. [CrossRef]

25. Kaur, A.; Singh, L.; Dhillon, J.S. Modified Krill Herd Algorithm for Constrained Economic Load Dispatch Problem. *Int. J. Ambient. Energy* 2022, 43, 4332–4342. [CrossRef]

26. Mohammadi, F.; Abdi, H. A Modified Crow Search Algorithm (MCSA) for Solving Economic Load Dispatch Problem. *Appl. Soft Comput. J.* 2018, 71, 51–65. [CrossRef]

27. Shen, X.; Wu, G.; Wang, R.; Chen, H.; Li, H.; Shi, J. A Self-Adapted Across Neighborhood Search Algorithm with Variable Reduction Strategy for Solving Non-Convex Static and Dynamic Economic Dispatch Problems. *IEEE Access* 2018, 6, 41314–41324. [CrossRef]

28. Li, F.; Qin, J.; Kang, Y. Multi-Agent System Based Distributed Pattern Search Algorithm for Non-Convex Economic Load Dispatch in Smart Grid. *IEEE Trans. Power Syst.* 2019, 34, 2093–2102. [CrossRef]

29. Yu, J.T.; Kim, C.H.; Wadood, A.; Khurshaid, T.; Rhee, S.B. Jaya Algorithm with Self-Adaptive Multi-Population and Lévy Flights for Solving Economic Load Dispatch Problems. *IEEE Access* 2019, 7, 21372–21384. [CrossRef]

30. Mokarram, M.J.; Niknam, T.; Aghaei, J.; Shafie-Khah, M.; Catalão, J.P.S. Hybrid Optimization Algorithm to Solve the Nonconvex Multiarea Economic Dispatch Problem. *IEEE Syst. J.* 2019, 13, 3400–3409. [CrossRef]

31. Tai, T.C.; Lee, C.C.; Kuo, C.C. A Hybrid Grey Wolf Optimization Algorithm Using Robust Learning Mechanism for Large Scale Economic Load Dispatch with Vale-Point Effect. *Appl. Sci.* 2023, 13, 2727. [CrossRef]

32. Dong, R.; Wang, S. New Optimization Algorithm Inspired by Kernel Tricks for the Economic Emission Dispatch Problem with Valve Point. *IEEE Access* 2020, 8, 16584–16594. [CrossRef]

33. Xin-gang, Z.; Ji, L.; Jin, M.; Ying, Z. An Improved Quantum Particle Swarm Optimization Algorithm for Environmental Economic Dispatch. *Expert Syst. Appl.* 2020, 152, 113370. [CrossRef]

34. Kansal, V.; Dhillon, J.S. Emended Salp Swarm Algorithm for Multiobjective Electric Power Dispatch Problem. *Appl. Soft Comput. J.* 2020, 90, 106172. [CrossRef]

35. Azeem, M.; Malik, T.N.; Muqeet, H.A.; Hussain, M.M.; Ali, A.; Khan, B.; Rehman, A. Combined Economic Emission Dispatch in Presence of Renewable Energy Resources Using CISSA in a Smart Grid Environment. *Electron* 2023, 12, 715. [CrossRef]

36. Hagh, M.T.; Kalajahi, S.M.S.; Ghorbani, N. Solution to Economic Emission Dispatch Problem Including Wind Farms Using Exchange Market Algorithm Method. *Appl. Soft Comput.* 2020, 88, 106044. [CrossRef]

37. Ali, M.H.; El-Rifaie, A.M.; Youssef, A.A.F.; Tulsky, V.N.; Tolba, M.A. Techno-Economic Strategy for the Load Dispatch and Power Flow in Power Grids Using Peafowl Optimization Algorithm. *Energies* **2023**, *16*, 846. [CrossRef]
38. Ellahi, M.; Abbas, G.; Satrya, G.B.; Usman, M.R.; Gu, J. A Modified Hybrid Particle Swarm Optimization with Bat Algorithm Parameter Inspired Acceleration Coefficients for Solving Eco-Friendly and Economic Dispatch Problems. *IEEE Access* **2021**, *9*, 82169–82187. [CrossRef]
39. Xu, M.; Li, W.; Feng, Z.; Bai, W.; Jia, L.; Wei, Z. Economic Dispatch Model of High Proportional New Energy Grid-Connected Consumption Considering Source Load Uncertainty. *Energies* **2023**, *16*, 1696. [CrossRef]
40. Kurundkar, K.M.; Vaidya, G.A. Stochastic Security-Constrained Economic Dispatch of Load-Following and Contingency Reserves Ancillary Service Using a Grid-Connected Microgrid during Uncertainty. *Energies* **2023**, *16*, 2607. [CrossRef]
41. Ma, H.; Yang, Z.; You, P.; Fei, M. Multi-Objective Biogeography-Based Optimization for Dynamic Economic Emission Load Dispatch Considering Plug-in Electric Vehicles Charging. *Energy* **2017**, *135*, 101–111. [CrossRef]
42. Zou, Y.; Zhao, J.; Ding, D.; Miao, F.; Sobhani, B. Solving Dynamic Economic and Emission Dispatch in Power System Integrated Electric Vehicle and Wind Turbine Using Multi-Objective Virus Colony Search Algorithm. *Sustain. Cities Soc.* **2021**, *67*, 102722. [CrossRef]
43. Liu, Z.F.; Li, L.L.; Liu, Y.W.; Liu, J.Q.; Li, H.Y.; Shen, Q. Dynamic Economic Emission Dispatch Considering Renewable Energy Generation: A Novel Multi-Objective Optimization Approach. *Energy* **2021**, *235*, 121407. [CrossRef]
44. Li, L.L.; Liu, Z.F.; Tseng, M.L.; Zheng, S.J.; Lim, M.K. Improved Tunicate Swarm Algorithm: Solving the Dynamic Economic Emission Dispatch Problems. *Appl. Soft Comput.* **2021**, *108*, 107504. [CrossRef]
45. Li, L.L.; Shen, Q.; Tseng, M.L.; Luo, S. Power System Hybrid Dynamic Economic Emission Dispatch with Wind Energy Based on Improved Sailfish Algorithm. *J. Clean. Prod.* **2021**, *316*, 128318. [CrossRef]
46. Kheshti, M.; Ding, L.; Ma, S.; Zhao, B. Double Weighted Particle Swarm Optimization to Non-Convex Wind Penetrated Emission/Economic Dispatch and Multiple Fuel Option Systems. *Renew. Energy* **2018**, *125*, 1021–1037. [CrossRef]
47. Pandit, N.; Tripathi, A.; Tapaswi, S.; Pandit, M. An Improved Bacterial Foraging Algorithm for Combined Static/Dynamic Environmental Economic Dispatch. *Appl. Soft Comput. J.* **2012**, *12*, 3500–3513. [CrossRef]
48. Liang, H.; Liu, Y.; Li, F.; Shen, Y. Dynamic Economic/Emission Dispatch Including PEVs for Peak Shaving and Valley Filling. *IEEE Trans. Ind. Electron.* **2019**, *66*, 2880–2890. [CrossRef]
49. Al-Bahrani, L.T.; Horan, B.; Seyedmahmoudian, M.; Stojcevski, A. Dynamic Economic Emission Dispatch with Load Dema Nd Management for the Load Demand of Electric Vehicles during Crest Shaving and Valley Filling in Smart Cities Environment. *Energy* **2020**, *195*, 116946. [CrossRef]
50. Behera, S.; Behera, S.; Barisal, A.K. Dynamic Combined Economic Emission Dispatch Integrating Plug-in Electric Vehicles and Renewable Energy Sources. *Int. J. Ambient. Energy* **2022**, *43*, 4683–4700. [CrossRef]
51. Wang, G.G.; Deb, S.; Coelho, L.D.S. Elephant Herding Optimization. In Proceedings of the 2015 3rd International Symposium on Computational and Business Intelligence (ISCBI), Bali, Indonesia, 7–9 December 2015; pp. 1–5. [CrossRef]
52. Wang, G.G.; Deb, S.; Gao, X.Z.; Dos Santos Coelho, L. A New Metaheuristic Optimisation Algorithm Motivated by Elephant Herding Behaviour. *Int. J. Bio-Inspired Comput.* **2016**, *8*, 394–409. [CrossRef]
53. Li, W.; Wang, G.G.; Alavi, A.H. Learning-Based Elephant Herding Optimization Algorithm for Solving Numerical Optimization Problems. *Knowl.-Based Syst.* **2020**, *195*, 105675. [CrossRef]
54. El-Naggar, M.F.; Mosaad, M.I.; Hasanien, H.M.; AbdulFattah, T.A.; Bendary, A.F. Elephant Herding Algorithm-Based Optimal PI Controller for LVRT Enhancement of Wind Energy Conversion Systems. *Ain. Shams. Eng. J.* **2021**, *12*, 599–608. [CrossRef]
55. Tariq, F.; Alelyani, S.; Abbas, G.; Qahmash, A.; Hussain, M.R. Solving Renewables-Integrated Economic Load Dispatch Problem by Variant of Metaheuristic Bat-Inspired Algorithm. *Energies* **2020**, *13*, 6225. [CrossRef]
56. Mukherjee, V.; Verma, S. Optimal Real Power Rescheduling of Generators for Congestion Management Using a Novel Ant Lion Optimiser. *IET Gener. Transm. Distrib.* **2016**, *10*, 2548–2561. [CrossRef]
57. Peesapati, R.; Yadav, V.K.; Kumar, N. Flower Pollination Algorithm Based Multi-Objective Congestion Management Considering Optimal Capacities of Distributed Generations. *Energy* **2018**, *147*, 980–994. [CrossRef]
58. Wulandhari, L.A.; Komsiyah, S.; Wicaksono, W. Bat Algorithm Implementation on Economic Dispatch Optimization Problem. *Procedia Comput. Sci.* **2018**, *135*, 275–282. [CrossRef]
59. Al-Betar, M.A.; Awadallah, M.A.; Krishan, M.M. A Non-Convex Economic Load Dispatch Problem with Valve Loading Effect Using a Hybrid Grey Wolf Optimizer. *Neural Comput. Appl.* **2020**, *32*, 12127–12154. [CrossRef]
60. Mohammadi-ivatloo, B.; Rabiee, A.; Soroudi, A.; Ehsan, M. Imperialist Competitive Algorithm for Solving Non-Convex Dynamic Economic Power Dispatch. *Energy* **2012**, *44*, 228–240. [CrossRef]
61. Lu, Y.; Zhou, J.; Qin, H.; Wang, Y.; Zhang, Y. Chaotic Differential Evolution Methods for Dynamic Economic Dispatch with Valve-Point Effects. *Eng. Appl. Artif. Intell.* **2011**, *24*, 378–387. [CrossRef]
62. Balamurugan, R.; Subramanian, S. Differential Evolution-Based Dynamic Economic Dispatch of Generating Units with Valve-Point Effects. *Electr. Power Compon. Syst.* **2008**, *36*, 828–843. [CrossRef]
63. Hemamalini, S.; Simon, S.P. Dynamic Economic Dispatch Using Artificial Immune System for Units with Valve-Point Effect. *Int. J. Electr. Power Energy Syst.* **2011**, *33*, 868–874. [CrossRef]
64. Immanuel Selvakumar, A. Enhanced Cross-Entropy Method for Dynamic Economic Dispatch with Valve-Point Effects. *Int. J. Electr. Power Energy Syst.* **2011**, *33*, 783–790. [CrossRef]

65. Yuan, X.; Su, A.; Yuan, Y.; Nie, H.; Wang, L. An Improved PSO for Dynamic Load Dispatch of Generators with Valve-Point Effects. *Energy* 2009, 34, 67–74. [CrossRef]
66. Victoire, T.A.A.; Jeyakumar, A.E. Deterministically Guided PSO for Dynamic Dispatch Considering Valve-Point Effect. *Electr. Power Syst. Res.* 2005, 73, 313–322. [CrossRef]
67. Sivasubramani, S.; Swarup, K.S. Hybrid SOA–SQP Algorithm for Dynamic Economic Dispatch with Valve-Point Effects. *Energy* 2010, 35, 5031–5036. [CrossRef]
68. Victoire, T.A.A.; Jeyakumar, A.E. Reserve Constrained Dynamic Dispatch of Units with Valve-Point Effects. *IEEE Trans. Power Syst.* 2005, 20, 1273–1282. [CrossRef]
69. Victoire, T.A.A.; Jeyakumar, A.E. A Modified Hybrid EP–SQP Approach for Dynamic Dispatch with Valve-Point Effect. *Int. J. Electr. Power Energy Syst.* 2005, 27, 594–601. [CrossRef]
70. Basu, M. Hybridization of Artificial Immune Systems and Sequential Quadratic Programming for Dynamic Economic Dispatch. *Electr. Power Compon. Syst.* 2009, 37, 1036–1045. [CrossRef]
71. He, D.; Dong, G.; Wang, F.; Mao, Z. Optimization of Dynamic Economic Dispatch with Valve-Point Effect Using Chaotic Sequence Based Differential Evolution Algorithms. *Energy Convers. Manag.* 2011, 52, 1026–1032. [CrossRef]